

Multiple Multidimensional Morse Wavelets

Statistics Section

Technical Report TR-05-02

June 8, 2018

Georgios Metikas & Sofia C. Olhede

Department of Mathematics, Imperial College London, SW7 2AZ UK

Abstract

We define a set of operators that localise a radial image in radial space and radial frequency simultaneously. We find the eigenfunctions of this operator and thus define a non-separable orthogonal set of radial wavelet functions that may be considered optimally concentrated over a region of radial space and radial scale space, defined via a doublet of parameters. We give analytic forms to their energy concentration over this region. We show how the radial function localisation operator can be generalised to an operator, localising any $L^2(\mathbb{R}^2)$ function. We show that the latter operator, with an appropriate choice of localisation region, approximately has the same eigenfunctions as the radial operator.

Based on the radial wavelets we define a set of quaternionic valued wavelet functions that can extract local orientation for discontinuous signals and both orientation and phase structure for oscillatory signals. The full set of quaternionic wavelet functions are component wise orthogonal; hence their statistical properties are tractable, and we give forms for the variability of the estimates of the local phase and orientation, as well as the local energy of the image. By averaging estimates across wavelets, a substantial reduction in the variance is achieved.

Index Terms

Scalogram, wavelets, image analysis, analytic signal, Riesz transform.

Manuscript received XXXXXXXX XX, XXXX; revised XXXXXXXX XX, XXXX. G. Metikas was supported by an EPSRC grant.

G. Metikas and S. Olhede are with the Department of Mathematics, Imperial College London, SW7 2AZ, London, UK (s.olhede@imperial.ac.uk). Tel: +44 (0) 20 7594 8568, Fax: +44 (0) 20 7594 8517.

I. INTRODUCTION

Localised analyses in one dimension have proven to be remarkably successful – notably so wavelet analyses. The latter is based on the idea that observed signals varying over an increasing argument, time say, exhibit disparate and highly localised behaviour associated with variations at a particular scale and at particular time points. Analysis is based on the wavelet transform, given for signal $g(t)$ using wavelet $\psi(t)$ via

$$\begin{aligned} w_\psi(a, b; g) &= \langle \psi_{a,b}, g \rangle \\ &= \int_{-\infty}^{\infty} g(t) |a|^{-1/2} \psi^* \left(\frac{t-b}{a} \right) dt, \end{aligned} \quad (1)$$

where a is referred to as the *scale*, b the *translation* and $*$ denotes conjugation. This allows for the recognition of patterns specific to time localisations b and length scales associated with scale a , if the function $\psi(\cdot)$ is chosen such that the support of $\psi(\cdot)$ is essentially limited to a region near the origin, and the support of the Fourier transform of $\psi(\cdot)$, is essentially limited to a region near some non-zero reference frequency f_{\max} . A function cannot be perfectly compact in time and frequency simultaneously, and so other criteria have been specified to determine the localisation properties of $\psi(\cdot)$. Of particular note is the idea of a localisation operator, generalizing the truncation in time or frequency operators [1] to *simultaneously* localising in time and frequency/scale [2], [3]. The eigenfunctions/eigenvectors of such operators are optimally localised with respect to the operator and in one dimension the problem of defining appropriate operators and calculating their eigenfunctions has been considered in detail [2], [3], [4].

The choice of extension of decomposition to two dimensional analysis is not trivial since variation in the spatial variable is associated with a direction, as well as a scale. This direction cannot be assumed to be aligned with the observational coordinate axes, and thus analysis using a simple tensor product of one-dimensional wavelets is, in general, not suitable. In two dimensions localisation is made to spatial point $\mathbf{b} = [b_1, b_2]^T$, in scale to a and in orientation to angle $\theta \in [0, 2\pi)$ cf [5]. The two dimensional continuous wavelet decomposition of image $g(\mathbf{x})$ using wavelet $\psi(\mathbf{x})$ is constructed via

$$\begin{aligned} w_\psi(a, \theta, \mathbf{b}; g) &= \langle \psi_{a,\theta,\mathbf{b}}, g \rangle \\ &= \int \int_{\mathbf{R}^2} g(\mathbf{x}) \psi_{a,\theta,\mathbf{b}}^*(\mathbf{x}) d^2\mathbf{x}, \end{aligned} \quad (2)$$

where (\mathcal{D}_a) represents a dilation, $(\mathcal{T}_{\mathbf{b}})$ a translation and (\mathcal{R}_θ) a rotation of $\psi(\mathbf{x})$ giving

$$\psi_{a,\theta,\mathbf{b}}(\mathbf{x}) = \mathcal{R}_\theta \mathcal{D}_a \mathcal{T}_{\mathbf{b}} \psi(\mathbf{x}) \quad (3)$$

$$= |a|^{-1} \psi(\mathbf{r}_{-\theta} a^{-1} (\mathbf{x} - \mathbf{b})), \quad (4)$$

with r_θ given as the rotation matrix. The decomposition will, with an appropriate choice of wavelet function, uncover/disentangle behaviour across specific spatial points, scales and orientation. Local two dimensional patterns in general may be intrinsically one dimensional, i.e. after a suitable rotation all variation is along a single axis, or intrinsically two dimensional, i.e. there is variation in several directions, operating at the same scale emanating from one spatial point. Following remarks by [6] we focus on wavelet analysis of discontinuities and oscillatory structure. Note that edges, or spatial discontinuities, have an orientation if they locally correspond to (one dimensional) curved discontinuities whilst (two dimensional) point discontinuities have no associated orientation. Oscillations may structurally take the form of one dimensional objects such as repeated lines with an even spacing that, if rotated to the appropriate axes, can be locally described as constant in one variable and as a sinusoid in the other. Two dimensional oscillations, circularly emanating from a single point, when considered locally at a distance from their source may be described approximately as one dimensional oscillations.

Thus the structure of an image is highly orientation dependent, and analysis methods should disentangle both locally one dimensional and two dimensional structures operating at many different orientations. A well known feature of wavelet analysis, [7] is that genuinely two dimensional structure, *i.e.* point discontinuities, are well represented in a wavelet decomposition, and so in this paper we focus instead on the treatment of locally one dimensional structures by adjusting the wavelet transform suitably. We shall discuss two existing strategies for considering oriented scale-based decompositions, and construct a new method corresponding to a synthesis of the two methods discussed. This method can extract the local orientation of the image explicitly, in a multi-scale framework.

Existing continuous wavelet methods that deal with the orientation of the image explicitly are based on directionally selective filters, or *directional wavelets*. Antoine & Murenzi [5] define complex directional wavelets with a preferred orientation in the frequency domain, as their frequency support is limited to a pre-defined cone, parameterised via the opening and closing angles of the cone [5, p. 324–5]. Defining highly directional wavelets will necessitate an elongation of the wavelets in the spatial frequency domain, and this affects their spatial and spatial frequency resolution capacity – along a specific orientation in the frequency domain, the wavelets localise badly in frequency, and for this reason we do not use directional wavelets. Directional wavelets will localise in scale *and* direction, whilst spatially isotropic wavelets only separate features at different scales. We shall use an isotropic wavelet decomposition to separate out disparate components occurring at either different scales and the same spatial locations, or at the same scales at different spatial locations. To facilitate this separation of structure, wavelets that are optimally concentrated in radial space and radial frequency are required, as in two dimensions

the notion of spatial distance is naturally associated with the Cartesian metric. We define a family of radial two-dimensional localisation operators and find the radial eigenfunctions of any given operator in this family, denoted the isotropic Morse wavelets. Any operator in this family is characterised via two parameters that determine the spatial/spatial frequency structure of the isotropic eigenfunctions. Any choice of the parameters fixes a particular operator that in turn possesses a family of eigenfunctions. These functions are orthogonal and indexed via n . The eigenvalues explicitly give the radial concentration of the eigenfunctions. These eigenfunctions are related (but not equivalent) to the eigenfunctions of the one dimensional Morse localisation operator [3]. For every fixed value of n , and given radial eigenfunction, we define an additional pair of functions, whose joint norm may be considered to have the same localisation in space and spatial scale as the original radial function, but when combined with the original radial function will disentangle the local orientation of the image analysed. These extra pairs of functions are constructed explicitly to consider local orientation and phase.

A method for considering local phase structure is to extend the notion of instantaneous frequency [8]; [9], [10], [11] give extensions to instantaneous frequency and local phase structure in the spatial domain, and for each spatial point retrieve a local phase/variational structure. These extensions correspond to the calculation of several additional images, or quadrature components, at each spatial point, where each additional set of components is considered to have the same local spatial energy and variational structure as the original image. The full set of components is used to calculate the local orientation and variational structure. The additional components are ill-defined when constructed from multi-component images, as then a single component with a spatially varying phase function is not an appropriate model for the original image. It thus becomes necessary to combine the calculation of a local phase with scale-localised methods such as the wavelet transform. For each fixed value $n \in \mathbb{N}$, for each Morse wavelet, we define two extra real functions to complement the isotropic Morse wavelets. The triplet of real valued functions form a monogenic signal [9]. Two of the triplet of functions should be thought of as a single vector valued object, where their vector structure characterises the orientation of the local variations. The monogenic wavelets and wavelet transform are best represented using quaternion [12], rather than, real or complex numbers. Each triplet is therefore considered as a positive real valued amplitude, a pure unit quaternion specifying a direction, and a phase. The real amplitude characterises a local energy, the pure unit quaternion an orientation, and the phase a local variational structure [9]. The quaternion algebra allows for easy parameterisation of phase and orientation structure.

In one dimension analytic wavelets, *i.e.* Cauchy or Morlet wavelets [13, p. 28], are used to identify local oscillatory structure, of a real image $g(\cdot)$. The monogenic Morse wavelets are the natural two-dimensional

extension of the analytic Morse wavelets [3], and they define a local phase and orientation structure at each spatial/spatial scale point for a two dimensional oscillatory image, yielding a natural, and more elegant, structure for wavelet ridge analysis [14]. Oscillatory images are the complements of discontinuous images, where the two kinds of images appear as either oscillatory or discontinuous depending on if they are analysed in the Fourier or spatial domain. We consider line, or curved, discontinuities that may locally be thought of as one dimensional structures, and discuss the retrieval of their local features. Analyses using the separable discrete wavelet transform in addition with local phase structure characterisations, have been previously considered [15], [16]. However, in contrast to their procedure, we define *multiple orthogonal continuous* wavelets, based on a different two dimensional extension to the analytic signal. The Morse wavelets are additionally optimally concentrated with respect to a radial position/scale region \mathcal{D} . Other quaternion valued decompositions includes the work of [17], however this decomposition is only suitable for deterministic images.

We briefly discuss the discrete implementation of the two dimensional monogenic Morse wavelet transform, and in more depth the statistical properties of the transform. Unavoidably, most observed signals are contaminated by noise, and so robust methods that can deal with noise must be designed. As the operator problem yields solutions of multiple orthogonal monogenic wavelets, we may use the notion of averaging uncorrelated estimates [1] to retrieve estimates of the space-scale energy as well as other quantities of the image with reduced variance. Multiple orthogonal filters have been considered in several dimensions for stationary processes [18], and non-stationary processes [19] using the windowed Fourier transform and tensor product windows, but our wavelets are in contrast to these methods orthogonal, *non-separable monogenic* wavelet functions. Finally, the methods are illustrated on typical examples, showing the power of the multiple monogenic Morse wavelets.

II. NOTATION

We denote the 1D Fourier transform of $g(\cdot)$, $G(f) = \langle \exp(2j\pi ft), g \rangle$, and the two dimensional Fourier transform of $g(\mathbf{x})$ as $G(\mathbf{f}) = \langle \exp(2j\pi \mathbf{f} \mathbf{x}), g \rangle$. We denote an arbitrary quaternion via $q = q_1 + q_2i + q_3j + q_4k$, where $q_i \in \mathbb{R}$, $i = 1, \dots, 4$ and note that $i^2 = j^2 = k^2 = ijk = -1$, whilst $ij = -ji = k$, $ik = -ki = -j$, and finally $jk = -kj = i$. The algebra is non-Abelian. We additionally define the two dimensional Fourier transform in terms of any unit quaternion as $G_{e_q}(\mathbf{f}) = \langle \exp(2e_q\pi \mathbf{f} \mathbf{x}), g \rangle$, so that the regular Fourier transform corresponds to $G_j(\mathbf{f}) \equiv G(\mathbf{f})$. For more notes on quaternion algebra see [12]. We retain here only the briefest possible usage of the quaternion algebra, necessary for clarity of exposition, and stress that all implementation is discussed in terms of real vector quantities. The rotation

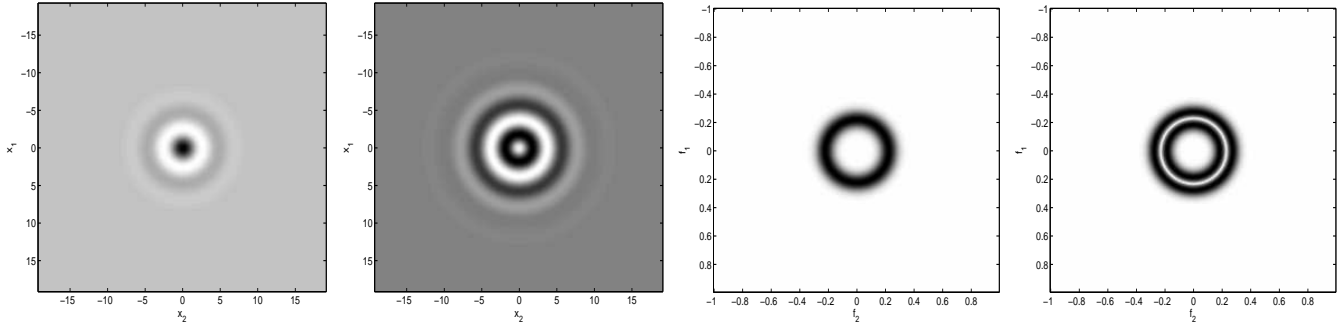


Fig. 1. The isotropic Morse wavelets in the spatial domain. $(l, m) = (8, 3)$ and $n = 0$ (far left), $n = 1$ (second from left). The modulus of the isotropic Morse wavelets in the spatial frequency domain. $(l, m) = (8, 3)$ and $n = 0$ (second from right), $n = 1$ (far right).

operation is implemented using matrix

$$r_\theta \equiv \begin{pmatrix} \cos(\theta) & -\sin(\theta) \\ \sin(\theta) & \cos(\theta) \end{pmatrix}.$$

We shall extensively use polar coordinates, and define: $\mathbf{x} = [x \cos(\chi), x \sin(\chi)]$, $\mathbf{f} = [f \cos(\phi), f \sin(\phi)]$, and $\mathbf{b} = [b \cos(\phi_b), b \sin(\phi_b)]$.

III. TWO DIMENSIONAL WAVELET ANALYSIS

One dimensional local analysis corresponds to decomposing a function in terms of a set of functions that contain behaviour local to a set scale a , and time point b . The two dimensional wavelet transform is defined using four parameters: $\boldsymbol{\xi} = [a, \theta, \mathbf{b}]$, where a and \mathbf{b} play roughly the same role as the corresponding one dimensional quantities, and θ corresponds to local orientation localisation. For the decomposition to be meaningful, the translated and dilated wavelets are chosen in one dimension to be mainly supported near time point b and frequency point $f_a = f_{\max}/a$, and the obvious extension to two dimensions would be to find functions that are mainly supported at spatial point \mathbf{b} and spatial frequency point $\mathbf{f}_a = \frac{f_{\max}}{a} [\cos(\theta), \sin(\theta)]$. To measure the localisation of a given wavelet function, commonly its spread in time and frequency or scale is calculated, and both quantities are desired to be low – their product is bounded below, thus restricting possible joint localisation. A function’s spread in time and frequency should be considered simultaneously in the two domains [3], rather than combining two separate marginal properties: for this purpose localisation operators were defined, denoted $\mathcal{P}_{\mathcal{D}}$. The localisation of a function $g(\cdot)$ to region \mathcal{D} is measured by the ratio of energy $\mu_g(\mathcal{D}) = \langle \mathcal{P}_{\mathcal{D}}g(\cdot), \mathcal{P}_{\mathcal{D}}g(\cdot) \rangle / \langle g(\cdot), g(\cdot) \rangle$, and the eigenfunctions of $\mathcal{P}_{\mathcal{D}}$ achieve optimal ratios [3]. Naturally extending analysis to two dimensions requires

the appropriate definition of a two-dimensional localisation operator. We consider localisation in scale and spatial location, which requires localisation in radial spatial frequencies of spatially radial functions, as we wish to associate a notion of distance to the Cartesian two dimensional metric. This produces functions optimally concentrated in a radial space and scale a , but that have no orientation. We then construct a set of functions capable of extracting local orientation information based on the monogenic signal [9]. [20] have shown that with an appropriate definition of scale, orientation and spatial spread, the orientation and scale may be considered separately when finding optimally concentrated functions. In a slightly different setting they demonstrate that radial functions have optimal scale versus position localisation properties, for appropriately chosen families of functions. This, in combination with a Cartesian metric in the plane, motivates the study of radial localisation.

A. Radial Localisation Operator

The construction of a coherent radial state, required for the construction of a radial projection operator, is not straightforward. We commence with radial function $v(\mathbf{x}) = v_r(x)$ and in theory wish to construct a family of radial functions that have been shifted in scale and position. Obviously this is impossible, as once we shift in position, we no longer have a radial function, but we may relax our requirements as the family only needs to act in a similar fashion to a direction averaged spatial shift, based on an appropriate domain \mathcal{D} chosen. To construct a generic two-dimensional non-radial coherent state we would use the full set of parameters $\boldsymbol{\xi} = [a, \theta, \mathbf{b}]$, but intend to use the sub-set $\boldsymbol{\xi}_r = [a, b]$. Working with radial functions the act of rotation, represented by θ will have little importance, and is not included. The dilation by a will act correspondingly in the world of radial operations, to one dimensional analysis, and a substitute for a shift in position by \mathbf{b} must be defined. We reconstruct the function using building blocks of $\langle v_{\boldsymbol{\xi}}, g \rangle v_{\boldsymbol{\xi}}$ that are averaged over suitably defined domains. The localisation domain will be defined in terms of b and range over $0 \leq \phi_b \leq 2\pi$. This implies that any shift in \mathbf{b} will be averaged over the full range of ϕ_b and so rather than multiplying $V(\mathbf{f})$ by $e^{-2\pi j \mathbf{f} \cdot \mathbf{b}}$ we could multiply this by its angular average of $J_0(2\pi f b)$, that after implementing the operator projection, yields the same results as the former strategy. Unfortunately, this choice of coherent state leads to a mathematically intractable operator, and so we define a radial coherent state for $a > 0$ and $b > 0$ that has similar properties to the suggested state via

$$V_{\boldsymbol{\xi}_r}^{(+)}(\boldsymbol{\omega}) = \sqrt{2} a^{1/\gamma} (a^{1/\gamma} \boldsymbol{\omega})^{-1/2 + \gamma/2} V^{\beta, \gamma}(a^{1/\gamma} \boldsymbol{\omega}) \frac{\cos(\boldsymbol{\omega}^\gamma b - \pi/4)}{\sqrt{\boldsymbol{\omega}^\gamma b}}, \quad (5)$$

based on the Morse coherent state [3] of

$$V^{\beta, \gamma}(\boldsymbol{\omega}) = \frac{2^{r/2+1/2} \sqrt{\pi \gamma}}{\sqrt{\Gamma(r)}} \boldsymbol{\omega}^\beta e^{-\boldsymbol{\omega}^\gamma} \quad \text{if } \boldsymbol{\omega} > 0.$$

Note that $V^{\beta,\gamma}(\omega) \propto \omega^\beta$, $\beta > 0$ for $\omega \ll 1$, and for future reference define $\omega_\epsilon : V^{\beta,\gamma}(\omega) < \epsilon \forall \omega < \omega_\epsilon$. In equation (5) the dilation of a is implemented as in [3] and requires no further discussion. The factor $(a^{1/\gamma}\omega)^{-1/2+\gamma/2}$ is added to ensure the correct normalisation of the two-dimensional radial function, as is the replacement of $a^{1/\gamma}$ for $a^{1/(2\gamma)}$, as the term in a multiplying the dilated function of ω . Denote the translation-like operator, and the originally posited direction averaged operator respectively as, $T_b^{(1)}(\omega, b) = \frac{\cos(\omega^\gamma b - \pi/4)}{\sqrt{\omega^\gamma b}}$, and $T_b^{(2)}(\omega, b) = J_0(\omega^\gamma b)$. The translation operator's decay for large values of $\omega^\gamma b$ is the same as $T_b^{(2)}(\omega, b)$, as is its zero crossing structure, and apart from small arguments the two functions are performing a similar action. The functional behaviour for small values of ω is different – $T_b^{(2)}(\omega, b) = 1 + O(\omega^{2\gamma})$ whilst $T_b^{(1)}(\omega, b) = \frac{1}{\sqrt{2\omega^\gamma b}} + O(\omega^\gamma)$, where the latter is unbounded near $\omega \rightarrow 0$. If we denote the coherent state as

$$V_{\xi_r}^{+(u)}(\omega) = \sqrt{2}a^{1/\gamma}(a^{1/\gamma}\omega)^{-1/2+\gamma/2}V^{\beta,\gamma}(a^{1/\gamma}\omega)T_b^{(u)}(\omega, b), \quad u = 1, 2,$$

then for small values of ω , with $r = (2\beta + 1)/\gamma$, we find

$$\begin{aligned} V_{\xi_r}^{+(u)}(\omega) &= \sqrt{\frac{2^{r+2}\pi\gamma}{\Gamma(r)}}a^{1/\gamma}(a^{1/\gamma}\omega)^{-1/2+\gamma/2}(a^{1/\gamma}\omega)^\beta [1 + O(\omega^\gamma)] T_b^{(u)}(\omega, b) \\ V_{\xi_r}^{+(1)}(\omega) &= C_1\omega^{\beta-1/2} + O(\omega^{-1/2+\gamma+\beta}) \\ V_{\xi_r}^{+(2)}(\omega) &= C_2\omega^{-1/2+\gamma/2+\beta} + O(\omega^\gamma), \end{aligned}$$

so that both choices give contributions of negligible magnitude for $|\omega| \rightarrow 0$ as long as we assume $\beta > 1/2$, which is combined with the previous constraint of $\gamma \geq 1$, with $\beta > (\gamma - 1)/2$ [3, p. 2663]. We choose $T_b^{(1)}$ as the radial spatial shift quantity. This has an approximate interpretation of b as a orientation averaged spatial shift. Note that the generalised Morse wavelets also are based on the approximate, rather than exact, notion of a *warped* location shift [3, p. 2663].

We define the operator for a radial function $g(x)$ in terms of radial inner product $\langle g_1, g_2 \rangle_R = \frac{1}{2\pi} \langle G_1, G_2 \rangle_R = \int G_1^*(f)G_2(f)f df$ as and (in terms of $\mathcal{D}^+(C) = \{(a, b) : a^2 + b^2 + 1 \leq 2aC, b > 0\}$),

$$\begin{aligned} \mathcal{P}_{\mathcal{D}^+} \{G\} \left(\frac{\omega_1}{2\pi} \right) &= C_o \int_{\mathcal{D}} V_{\xi}^+(\omega_1) \langle V_{\xi}^+, G \rangle \frac{da}{a^2} db \\ &= C_o \int_{\omega_2=0}^{\infty} \int \int_{a^2+b^2+1 \leq 2aC} \kappa_2(\omega_1, \omega_2; a, b) \frac{da}{a^2} db d\omega_2, \end{aligned} \quad (6)$$

where

$$\kappa_2(\omega_1, \omega_2; a, b) = 2a^{1/\gamma}V^{\beta,\gamma}(a^{1/\gamma}\omega_1)\sqrt{\omega_2/\omega_1}V^{\beta,\gamma}(a^{1/\gamma}\omega_2)G\left(\frac{\omega_2}{2\pi}\right)\cos((\omega_1^\gamma - \omega_2^\gamma)b). \quad (7)$$

The kernel $\kappa_2(\cdot, \cdot; \cdot, \cdot)$ can be inverted in its first argument to retrieve the spatial domain operator. Note that by definition $\omega_1 > 0$. We constrain the norm of the operator – exactly reconstructing the entire radial

function if we let the region of integration across ξ_r be large enough, thus calibrating the operator to make the eigenvalues meaningful.

$$\begin{aligned}
G\left(\frac{\omega_1}{2\pi}\right) &= C_o \int_{\omega_2=0}^{\infty} \int_{a=0}^{\infty} \int_{b=0}^{\infty} 2a^{1/\gamma} V^{\beta,\gamma}(a^{1/\gamma}\omega_1) \sqrt{\omega_2/\omega_1} V^{\beta,\gamma}(a^{1/\gamma}\omega_2) \\
&\quad G\left(\frac{\omega_2}{2\pi}\right) \cos((\omega_1^\gamma - \omega_2^\gamma)b) \frac{da}{a^2} db d\omega_2 \\
&= C_o \int_{\omega_2=0}^{\infty} \int_{a=0}^{\infty} \int_{b=-\infty}^{\infty} a^{1/\gamma} V^{\beta,\gamma}(a^{1/\gamma}\omega_1) \sqrt{\omega_2/\omega_1} V^{\beta,\gamma}(a^{1/\gamma}\omega_2) \\
&\quad G\left(\frac{\omega_2}{2\pi}\right) \cos((\omega_1^\gamma - \omega_2^\gamma)b) \frac{da}{a^2} db d\omega_2 \\
&= C_o 2(2\pi)^2 G\left(\frac{\omega_1}{2\pi}\right) \frac{1}{r-1}, \tag{8}
\end{aligned}$$

which gives $C_o = \frac{r-1}{2^3\pi^2}$, yielding a ‘resolution of identity’ [3] for radial functions: this will *not* hold for any $g(\cdot) \in L^2(\mathbb{R}^2)$, as the operator is *only* defined for radial functions. The eigenfunctions of the operator defined in (6) can be found by solving the equation

$$\mathcal{P}_{\mathcal{D}^+} \{G\} \left(\frac{\omega_1}{2\pi}\right) = \lambda G\left(\frac{\omega_1}{2\pi}\right). \tag{9}$$

The one-dimensional Morse wavelet projection operator can be considered to be in the case of $\psi(t)$ real, assuming that $\omega_1 > 0$, (similar expressions are derived for $\omega_1 < 0$, but as we shall use this to obtain solutions to equation (9) we only need to consider $\omega_1 > 0$, and the $\sin(\cdot)$ term vanishes due to the symmetry of the projection region, and where \mathcal{D} is as in [3]):

$$\begin{aligned}
\mathcal{P}_{\mathcal{D}}^{1D} \{\Psi\} \left(\frac{\omega_1}{2\pi}\right) &= C_o^{1D} \int_{\omega_2=0}^{\infty} \int \int_{a^2+b^2+1 \leq 2aC, a \in R^+, b \in R} a^{1/\gamma} V^{\beta,\gamma}(a^{1/\gamma}\omega_1) V^{\beta,\gamma}(a^{1/\gamma}\omega_2) \tag{10} \\
&\quad \Psi\left(\frac{\omega_2}{2\pi}\right) \cos[b(\omega_1^\gamma - \omega_2^\gamma)] \frac{da}{a^2} db \frac{d\omega_2}{2\pi} \\
&= \frac{C_o^{1D}}{2\pi} \int_{\omega_2=0}^{\infty} \int \int_{a^2+b^2+1 \leq 2aC, a \in R^+, b \in R^+} \kappa_1(\omega_1, \omega_2, a, b) \frac{da}{a^2} db d\omega_2,
\end{aligned}$$

where

$$\kappa_1(\omega_1, \omega_2; a, b) = 2a^{1/\gamma} V^{\beta,\gamma}(a^{1/\gamma}\omega_1) V^{\beta,\gamma}(a^{1/\gamma}\omega_2) \Psi\left(\frac{\omega_2}{2\pi}\right) \cos((\omega_1^\gamma - \omega_2^\gamma)b). \tag{11}$$

Note that the above kernel $\kappa_1(\cdot, \cdot; \cdot, \cdot)$ is similar to the kernel $\kappa_2(\cdot, \cdot; \cdot, \cdot)$ of (7), the only difference being that $\kappa_2(\cdot, \cdot; \cdot, \cdot)$ has the extra term, $\sqrt{\omega_2/\omega_1}$, and $C_o^{1D} = \frac{r-1}{4\pi}$. The Morse wavelets [3] are the solution to the equation

$$\mathcal{P}_{\mathcal{D}}^{1D} \{\Psi\} \left(\frac{\omega_1}{2\pi}\right) = \lambda^{1D} \Psi\left(\frac{\omega_1}{2\pi}\right). \tag{12}$$

Consider equation (9); multiply both sides by $\sqrt{\omega_1/(2\pi)}$, set $G(\omega)\sqrt{\omega} = \Psi(\omega)$, and note that the equation to be solved has now exactly the form of equation (12):

$$\begin{aligned} \sqrt{\frac{\omega_1}{2\pi}} \mathcal{P}_{\mathcal{D}^+} \{G\} \left(\frac{\omega_1}{2\pi}\right) &= \mathcal{P}_{\mathcal{D}^+} \{\Psi\} \left(\frac{\omega_1}{2\pi}\right) = \frac{2\pi C_o}{C_o^{1D}} \mathcal{P}_{\mathcal{D}}^{1D} \{\Psi\} \left(\frac{\omega_1}{2\pi}\right) \\ &= \lambda^{1D} \Psi\left(\frac{\omega_1}{2\pi}\right), \end{aligned} \quad (13)$$

where we have used that $2\pi C_o/C_o^{1D} = 1$. Thus the solutions of (9) are given by

$$\Psi_{n;l,m}^{2D}(\mathbf{f}) = \frac{1}{\sqrt{f}} \Psi_{n;\beta,\gamma}^{(e)}(f), \quad f > 0, \quad (14)$$

where $\Psi_{n;\beta,\gamma}^{(e)}(\cdot)$ are the even Morse wavelets as defined in one dimension [3], $l = \beta - \frac{1}{2}$, $m = \gamma$, and $n \in N$ enumerates the eigenvectors. The eigenvalues correspond to,

$$\lambda_{n,r}(C) = \lambda_{n,r}^{1D} = \frac{\Gamma(r+n)}{\Gamma(n+1)\Gamma(r-1)} \int_0^{\frac{C-1}{C+1}} x^n (1-x)^{r-2} dx, \quad (15)$$

and this yields the radial-spatial, radial-scale concentration of $\mu_{\psi_n^{(e)}}(\mathcal{D}(C)) = \lambda_{n,r}^2(C)$. It may seem surprising that, in two-dimensions, the same eigenvalues, and thus concentration values, are found as in the one-dimensional case, note, however, that this is only derived for radial images, that are constrained to the same behaviour in both spatial directions – hence in essence we are really only making a one dimensional compromise. The *hypervolume* of \mathcal{D} is directly related to C , and note that we may formulate the notion of bias of estimation of local properties of the signal, or leakage, in terms of the eigenvalues as $1 - \lambda_{n,r}^2(C)$ [3].

B. Non-Radial Localisation Operators

The operator outlined above was constructed in the radial frequency domain for explicitly radial images. Let us explicitly consider how a operator is constructed in two dimensions. Define

$$\mathcal{D}_2 = \{\boldsymbol{\xi} : a^2 + b^2 + 1 \leq aC, 0 \leq \theta \leq 2\pi, \mathbf{b} \in \mathbb{R}^2, a > 0\}. \quad (16)$$

Let us again consider a coherent state $\tilde{v}_{\boldsymbol{\xi}}^+(\mathbf{x})$ that is the building block of the projection operator, but let us now make this local to $\boldsymbol{\xi}$. Define the Fourier transform of this coherent state at $\boldsymbol{\xi}$ with $2\pi\mathbf{f} = \boldsymbol{\omega}$ as

$$\begin{aligned} \tilde{V}_{\boldsymbol{\xi}}^+(\boldsymbol{\omega}) &= a^{1/(2\gamma)+1/2} \omega^{-1/2+\gamma/2} V^{\beta,\gamma}(a^{1/\gamma}\omega) e^{-j\mathbf{b}(\mathbf{r}-\theta\boldsymbol{\omega})\omega^{\gamma-1}} \\ &= \frac{2^{(r+1)/2} \sqrt{\pi\gamma}}{\Gamma(r)} a^{(r+1)/2} \omega^{-1/2+\gamma/2} \omega^\beta e^{-a\omega^\gamma - j\mathbf{b}(\mathbf{r}-\theta\boldsymbol{\omega})\omega^{\gamma-1}}. \end{aligned} \quad (17)$$

The normalization of \tilde{V}^+ , for completeness, can be calculated by:

$$\langle \tilde{v}_{\boldsymbol{\xi}}^+, \tilde{v}_{\boldsymbol{\xi}}^+ \rangle = a^{1/\gamma+1} \frac{1}{(2\pi)^2} \int_0^\infty \int_0^{2\pi} \omega^{-1+\gamma} V^{\beta,\gamma^2}(a^{1/\gamma}\omega) \omega d\omega d\phi = \frac{r}{2}. \text{ Therefore, the coherent states are of}$$

norm unity, if they are multiplied by $\sqrt{\frac{2}{r}}$. We define the localisation operator for *any* function $g(\mathbf{x}) \in L^2(\mathbb{R}^2)$ as

$$\tilde{\mathcal{P}}_{\mathcal{D}_2} \{g\}(\mathbf{x}) = \tilde{C}_o \int_{\mathcal{D}_2} \tilde{v}_{\xi}^+(\mathbf{x}) \langle \tilde{v}_{\xi}^+, g \rangle \frac{da}{a^3} d^2b d\theta. \quad (18)$$

Equation (18) gives an expression for the localisation of an arbitrary function $g(\cdot)$ over region \mathcal{D}_2 . We can by calculating $\mu_g(\mathcal{D}_2)$ find the localisation of $g(\cdot) \in L^2(\mathbb{R}^2)$, to \mathcal{D}_2 . We shall take \tilde{C}_o such that as $|\mathcal{D}_2| \rightarrow \infty$, $\tilde{\mathcal{P}}_{\mathcal{D}_2} \{g\}(x) \rightarrow g(x)$ for all *radially symmetric* functions. Note that if $g(\cdot)$ is a radially symmetric function, then $\langle \tilde{v}_{\xi}^+, g \rangle = \frac{1}{(2\pi)} \int_0^\infty a^{1/(2\gamma)+1/2} \omega^{-1/2+\gamma/2} V^{\beta,\gamma}(a^{1/\gamma}\omega) G(\frac{\omega}{2\pi}) J_0(\omega^\gamma b) \omega d\omega$, where $J_0(\cdot)$ is the zeroth Bessel function [21]. Integration over ϕ , for a radial $g(\cdot)$, thus removes the angular dependence on θ and ϕ_b , see [22]. In the frequency domain

$$\begin{aligned} \tilde{\mathcal{P}}_{\mathcal{D}_2} \{G\}(\omega_1) &= \tilde{C}_o \int_{\mathcal{D}} \tilde{V}_{\xi}^+(\omega_1) \langle \tilde{V}_{\xi}^+, G \rangle \frac{da}{a^3} d^2b d\theta \\ &= 2\pi \tilde{C}_o \int_{\omega=0}^\infty \int \int_{a^2+b^2+1 \leq 2aC} a^{1/(2\gamma)+1/2} \omega_1^{-1/2+\gamma/2} V^{\beta,\gamma}(a^{1/\gamma}\omega_1) \omega_2^{1/2+\gamma/2} a^{1/(2\gamma)+1/2} \\ &\quad \times V^{\beta,\gamma}(a^{1/\gamma}\omega_2) G(\frac{\omega_2}{2\pi}) J_0(b\omega_1^\gamma) J_0(b\omega_2^\gamma) \frac{da}{a^3} b db d\omega_2 \end{aligned} \quad (19)$$

$$= \tilde{C}_o \int_{\omega_2 > 0} \int \int_{a^2+b^2+1 \leq 2aC} \kappa(\omega_1, \omega_2; a, b) \frac{da}{a^2} db d\omega_2. \quad (20)$$

Note that $V^{\beta,\gamma}(\omega) \approx 0$ if $\omega < \omega_\epsilon$ and thus we consider the term $J_0(\omega_l^\gamma b)$ for $\omega_l^\gamma b \gg 0$, as the point $b = 0$ has zero measure in the plane. For $|z| \gg 0$ the asymptotic approximation to the zeroth Bessel function is

$$J_0(z) \approx \frac{\sqrt{2}}{\sqrt{\pi z}} \cos(z - \frac{\pi}{4}),$$

cf [21, p. 364, 8.2.1]. We require $|\arg z| < \pi$ however, this is not an issue as $b > 0$ and $\omega_l > 0$. Thus for fixed non-zero b for values such that the integrand is non-zero

$$\begin{aligned} \kappa(\omega_1, \omega_2; a, b) &= 2\pi a^{1/\gamma} \omega_1^{-1/2+\gamma/2} V^{\beta,\gamma}(a^{1/\gamma}\omega_1) \omega_2^{1/2+\gamma/2} V^{\beta,\gamma}(a^{1/\gamma}\omega_2) G(\frac{\omega_2}{2\pi}) \\ &\quad J_0(b\omega_1^\gamma) J_0(b\omega_2^\gamma) b \\ &\approx 2\pi a^{1/\gamma} \omega_1^{-1/2+\gamma/2} V^{\beta,\gamma}(a^{1/\gamma}\omega_1) \omega_2^{1/2+\gamma/2} V^{\beta,\gamma}(a^{1/\gamma}\omega_2) G(\frac{\omega_2}{2\pi}) \\ &\quad b \sqrt{\frac{2}{\pi \omega_2^\gamma b}} \cos(\omega_2^\gamma b - \frac{\pi}{4}) \sqrt{\frac{2}{\pi \omega_1^\gamma b}} \cos(\omega_1^\gamma b - \frac{\pi}{4}) \\ &= 2a^{1/\gamma} V^{\beta,\gamma}(a^{1/\gamma}\omega_1) \sqrt{\omega_2/\omega_1} V^{\beta,\gamma}(a^{1/\gamma}\omega_2) G(\frac{\omega_2}{2\pi}) \cos((\omega_1^\gamma - \omega_2^\gamma)b) \\ &\quad + 2a^{1/\gamma} V^{\beta,\gamma}(a^{1/\gamma}\omega_1) \sqrt{\omega_2/\omega_1} V^{\beta,\gamma}(a^{1/\gamma}\omega_2) G(\frac{\omega_2}{2\pi}) \cos((\omega_1^\gamma + \omega_2^\gamma)b - \frac{\pi}{2}). \end{aligned} \quad (21)$$

The integration is over $\omega_2 > 0$ and also $\omega_1 > 0$, hence the first term of (21) dominates over the second term. The integrand of $\kappa(\omega_1, \omega_2; a, b)$ can be replaced by $\kappa_2(\omega_1, \omega_2; a, b)$ defined in (7) of the previous

section. Thus we approximate the operator acting on $G(\cdot)$ in the frequency domain via

$$\tilde{\mathcal{P}}_{\mathcal{D}_2} \{G\}(\boldsymbol{\omega}_1) \approx \tilde{C}_o \int_{\omega_2=0}^{\infty} \int \int_{a^2+b^2+1 \leq 2aC} \kappa_2(\omega_1, \omega_2; a, b) \frac{da}{a^2} db d\omega_2 \equiv \mathcal{P}_{\mathcal{D}} \{G\}(\boldsymbol{\omega}_1), \quad (22)$$

and \tilde{C}_o can be found from C_o . Defining $\tilde{\mathcal{P}}_{\mathcal{D}_2}$ allows for the consideration of the localisation of an arbitrary $L^2(\mathbb{R}^2)$ function. The radial eigenfunctions of $\tilde{\mathcal{P}}_{\mathcal{D}_2}$ are approximately those of $\mathcal{P}_{\mathcal{D}}$, where the derivation of the approximation shows the reasoning behind the definition of $\mathcal{P}_{\mathcal{D}}$. Finally $\tilde{\mathcal{P}}_{\mathcal{D}_2}$ can be generalised to an arbitrary localisation by removing the constraint of radial symmetry in \mathcal{D}_2 and on $g(\cdot)$.

C. Isotropic Wavelet Definition

The even multiple Morse wavelets are defined in one dimension in the Fourier domain for fixed $n = 0, 1, 2, \dots, \beta \geq 1, \gamma > (\beta-1)/2$ and denoted by $\Psi_{n;\beta,\gamma}^{(e)}(f)$ in terms of $A_{n;\beta,\gamma} = \sqrt{\pi\gamma 2^r \Gamma(n+1)/\Gamma(n+r)}$ [3]. We define the isotropic two dimensional wavelets as the eigenfunctions of $\mathcal{P}_{\mathcal{D}}$, for fixed n, l, m in terms of $f = \|\mathbf{f}\|$ via

$$\Psi_{n;l,m}^{(e)}(\mathbf{f}) = \frac{A_{n;l,m}}{\sqrt{\pi}} (2\pi f)^l e^{-(2\pi f)^m} L_n^{c'_{l,m}}(2(2\pi f)^m), \quad (23)$$

with $c'_{l,m} = (2l+2)/m - 1$, to attain the correct normalisation over $L^2(\mathbb{R}^2)$ and where $L_n^c(\cdot)$ are generalized Laguerre polynomials. The spatial domain wavelets with $x = \|\mathbf{x}\|$ are found via the inverse Fourier transform for radial images, $\psi_n^{(e)}(\mathbf{x}) = 2\pi \int_0^\infty \Psi^{(e)}(f) J_0(2\pi f x) f df$. We plot the wavelets for $l = 8$ and $m = 3$ with $n = 0, 1$ in the spatial domain, see Figure 1. Their radially symmetric oscillatory structure is very clear. They are optimally concentrated in a radial structure centred at the origin. We plot the modulus of the same function in the spatial frequency domain in the same plot. These functions are band-pass filters that are non-zero for a range of frequencies centred at the same distance from the origin in the frequency domain. The trough in the $n = 1$ follows as the first two wavelets are orthogonal, and we see that the sum of the moduli will be large in the same ring-shape structure. To further characterise the Morse wavelets define the radial frequency that maximises the isotropic Morse wavelets as

$$f_{\max}^{(n)} = \arg_{f>0} \max \left| \Psi_n^{(e)} \right|^2, \quad n = 0, \dots, N-1. \quad (24)$$

The magnitude square of the Fourier transform of analysis wavelet $\psi_{\boldsymbol{\xi},n}^{(e)}(\cdot)$ will have a maximum at frequency $f_{\max}^{(n)}/a$ and is unaffected by both \mathbf{b} and the rotation.

IV. MONOGENIC IMAGES

In one dimension the analytic signal is used to unambiguously define the phase and amplitude of a given real signal and using an analytic analysis wavelet will allow for the definition of a local magnitude

and phase at each time and scale point – a necessity for the analysis of multi-component images. The analytic signal is constructed in one dimension by removing all negative frequencies in the signal, and then inverting the Fourier transform – any real signal $u(t)$ is complemented by its Hilbert transform $v(t) = \mathcal{H}\{u\}(t)$, and the analytic signal corresponds to $u^+(t) = u(t) + iv(t)$. If an oscillation is persistent at a particular range of times, then it will be heavily weighted in the Fourier domain, and the analytic signal will approximately take the form of a complex exponential.

The correct extension of the analytic signal to two dimensions has been the subject of much debate – of particular note are perhaps the single orthant image of [11], the hypercomplex signal of [10] and the monogenic signal of [9]. Following Felsberg and Sommer [9] we define the Riesz transform of an image $u(\mathbf{x})$ as

$$\mathcal{R}u(\mathbf{x}) = i\mathcal{R}_1u(\mathbf{x}) + j\mathcal{R}_2u(\mathbf{x}) = iv^{(1)}(\mathbf{x}) + jv^{(2)}(\mathbf{x}). \quad (25)$$

The Fourier transforms of these two objects are

$$\mathcal{F}\{\mathcal{R}_1u(\mathbf{x})\} = -j \cos(\phi)U(\mathbf{f}), \quad \mathcal{F}\{\mathcal{R}_2u(\mathbf{x})\} = -j \sin(\phi)U(\mathbf{f}).$$

Define the monogenic image [9] as $u^{(+)}(\mathbf{x}) = u(\mathbf{x}) + \mathcal{R}u(\mathbf{x})$. This is a quaternion valued object, and relations between the components of the quaternion are interpretable in terms of orientation and phase, for oscillatory images, as will be demonstrated.

Consider an oscillation in two dimensions, corresponding to repeating maxima spaced $1/f_0$ apart in orientation $\mathbf{n} = [\cos(\eta) \ \sin(\eta)]^T$. This corresponds to the simplest oscillatory image

$$g_1(\mathbf{x}) = a_1 \cos(2\pi f_0 \mathbf{x} \cdot \mathbf{n} + \theta_s), \quad (26)$$

where a_1 , f_0 and θ_s are constant scalars, whilst \mathbf{n} is a constant unit length vector. Note that in variable $y = \mathbf{x} \cdot \mathbf{n}$, $g_1(\mathbf{x})$ solves the one dimensional harmonic oscillator equation of $\left[\frac{\partial^2}{\partial y^2} + (2\pi f_0)^2\right]g_1(y) = 0$. To characterise a given image, we wish to determine a_1 , f_0 , θ_s and \mathbf{n} , from the image.

We can calculate the monogenic extension of (26), and obtain, with $\mathbf{e}_\eta = i \cos(\eta) + j \sin(\eta)$, [23]

$$\begin{aligned} g_1^{(+)}(\mathbf{x}) &= g(\mathbf{x}) + ig^{(1)}(\mathbf{x}) + jg^{(2)}(\mathbf{x}) \\ &= a_1 [\cos(2\pi f_0 \mathbf{x} \cdot \mathbf{n} + \theta_s) + \mathbf{e}_\eta \sin(2\pi f_0 \mathbf{x} \cdot \mathbf{n} + \theta_s)]. \end{aligned} \quad (27)$$

In quaternionic polar coordinates,

$$g_1^{(+)}(\mathbf{x}) = a_1 e^{2\pi \mathbf{e}_\eta (f_0 y + \theta_s)}, \quad (28)$$

and we may determine $a_1 = \sqrt{g^2(\mathbf{x}) + g^{(1)2}(\mathbf{x}) + g^{(2)2}(\mathbf{x})}$, $\eta = \tan^{-1}\left(\frac{g^{(2)}(\mathbf{x})}{g^{(1)}(\mathbf{x})}\right)$, $f_0 y + \theta_s = \frac{1}{2\pi} \tan^{-1}\left(\frac{\text{sgn}(g^{(1)}(\mathbf{x}))\sqrt{g^{(1)2}(\mathbf{x}) + g^{(2)2}(\mathbf{x})}}{g(\mathbf{x})}\right)$. We restrict $-\frac{\pi}{2} < \eta < \frac{\pi}{2}$, and $-\frac{1}{2} < f_0 y +$

$\theta_s \leq \frac{1}{2}$. In terms of y we hence have a frequency domain description that perfectly mirrors the one dimensional theory, and retrieve the properties of the image from its monogenic extension. Naturally, in most real applications perfectly oscillatory images are not encountered, and more general models must be considered.

V. AM/FM/OM IMAGES

As in [14] and [24], we shall consider images that locally may be approximated as a sum of sinusoidal components. This model is of some importance in machine vision, and can be applied to granular flow and general oriented patterns [25]. Assume that

$$c(\mathbf{x}) = \sum_{l=1}^L c_l(\mathbf{x}), \quad c_l(\mathbf{x}) = a_l(\mathbf{x}) \cos(2\pi\phi_l(\mathbf{x})), \quad (29)$$

where $\phi_l(\mathbf{x}) = \varphi_l(\mathbf{n}_l(\mathbf{x}) \cdot \mathbf{x})$, with the added constraint that the unit vector $\mathbf{n}_l(\mathbf{x})$ is varying slowly, in comparison with \mathbf{x} , across the spatial period. We introduce this extra notation so that we may characterise images that can be considered as approximately sinusoidal in variable $y_l(\mathbf{x}) = \mathbf{n}_l(\mathbf{x}) \cdot \mathbf{x}$. We refer to $\mathbf{n}_l(\mathbf{x})$ as the orientation modulation (OM), whilst $\varphi_l(\cdot)$ is the phase modulation of component l , and plays the same role as the phase/frequency modulation (FM) of a one dimensional signal. Then we find that for $\mathbf{x} = \mathbf{x}_o + \delta\mathbf{x}$, and $\varphi'_l(y_l) = d/dy_l [\varphi_l(y_l)]$, that

$$\phi_l(\mathbf{x}) = \phi_l(\mathbf{x}_o) + \varphi'_l(\mathbf{n}_l(\mathbf{x}_o) \cdot \mathbf{x}_o) \mathbf{n}_l(\mathbf{x}_o) \cdot (\mathbf{x} - \mathbf{x}_o) + O(|\delta\mathbf{x}|^2). \quad (30)$$

In the following we will use the shorthand $\phi'_l(\mathbf{x}) = \varphi'_l(\mathbf{n}_l(\mathbf{x}) \cdot \mathbf{x})$. We additionally assume $a_l(\mathbf{x})$ varies slowly in comparison to the cosine term, and this corresponds to the amplitude modulation (AM). The monogenic version of the l th component is

$$\begin{aligned} c_l^+(\mathbf{x}) &= a_l(\mathbf{x}_o) e^{2\pi e_l(\mathbf{x}_o)(\phi_l(\mathbf{x}_o) + \phi'_l(\mathbf{x}_o) \mathbf{n}_l(\mathbf{x}_o) \cdot (\mathbf{x} - \mathbf{x}_o) + O(|\mathbf{x} - \mathbf{x}_o|^2))} \\ &= a_l(\mathbf{x}_o) \left[\cos \left(2\pi\phi_l(\mathbf{x}_o) + 2\pi\phi'_l(\mathbf{x}_o) \mathbf{n}_l(\mathbf{x}_o) \cdot (\mathbf{x} - \mathbf{x}_o) \right) \right. \\ &\quad \left. + e_l(\mathbf{x}_o) \sin \left(2\pi\phi_l(\mathbf{x}_o) + 2\pi\phi'_l(\mathbf{x}_o) \mathbf{n}_l(\mathbf{x}_o) \cdot (\mathbf{x} - \mathbf{x}_o) \right) \right] + o(|\mathbf{x} - \mathbf{x}_o|). \end{aligned} \quad (31)$$

cf equation (27). Assuming the orientation $e_l(\mathbf{x}_o)$ to be stable across values of \mathbf{x} for which $a_l(\mathbf{x})$ is non-zero, we shall perform the Fourier transform of $c_l^{(+)}(\mathbf{x})$ in terms of the unit quaternion $e_l(\mathbf{x}_o)$ instead of \mathbf{j} . Note that de Moivre's theorem is still valid for any unit quaternion, and so this directional Fourier transform can be interpreted just like the regular Fourier transform in terms of oscillatory components. The directional Fourier transform is then given by

$$C_{e_l, l}^+(\mathbf{f}) = \int \int a_l(\mathbf{x}_o) e^{2\pi e_l(\mathbf{x}_o)(\phi_l(\mathbf{x}_o) + \phi'_l(\mathbf{x}_o) \mathbf{n}_l(\mathbf{x}_o) \cdot (\mathbf{x} - \mathbf{x}_o))} e^{-2\pi e_l(\mathbf{x}_o) \mathbf{f} \cdot \mathbf{x}} d^2\mathbf{x}. \quad (32)$$

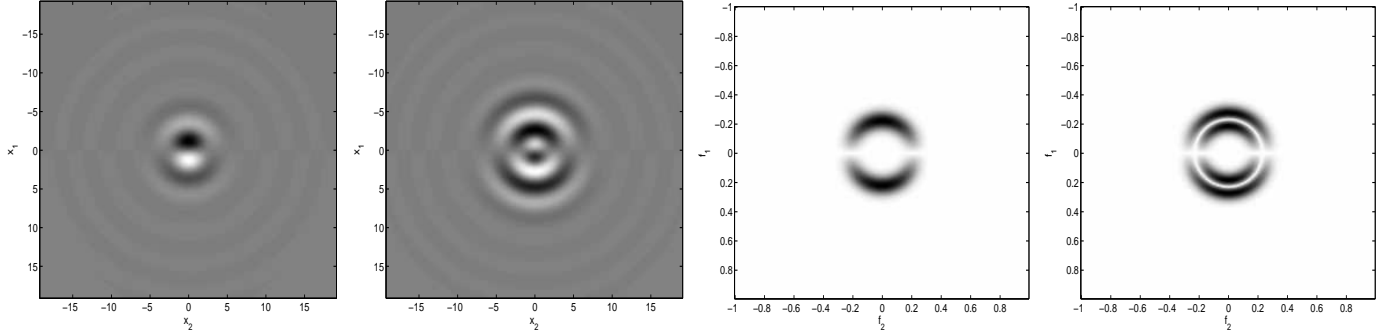


Fig. 2. The x_1 Riesz transform Morse wavelets in the spatial domain for $(l, m) = (8, 3)$ and $n = 0$ (far left), $n = 1$ (second left). The modulus of the x_1 Riesz transform Morse wavelets in the spatial frequency domain for $(l, m) = (8, 3)$ and $n = 0$, (second from right) $n = 1$ (far right).

We apply the stationary phase approximation to this integral [14], as the unit quaternion will be acting like \mathbf{j} itself. Thus, under the assumption that $\Omega(\mathbf{x}, \mathbf{f}) = \phi_l(\mathbf{x}_o) + \phi'_l(\mathbf{x}_o)\mathbf{n}_l(\mathbf{x}_o) \cdot (\mathbf{x} - \mathbf{x}_o) - \mathbf{f}\mathbf{x}$ has the unique stationary point \mathbf{x}_o , and there is quadratic behaviour around this point, i.e. $\Omega(\mathbf{x}, \mathbf{f}) = \frac{1}{2}[(\mathbf{x} - \mathbf{x}_o)\mathbf{H}(\mathbf{x} - \mathbf{x}_o)]$, where \mathbf{H} is the Hessian matrix of $\Omega(\mathbf{x}, \mathbf{f})$, we find at $\mathbf{f}(\mathbf{x}_o) = \phi'_l(\mathbf{x}_o)\mathbf{n}_l(\mathbf{x}_o)$, the integral provides the only non-null contribution of $C^+(\mathbf{f}) \approx \frac{2\pi}{\sqrt{|\mathbf{H}|}}a_l(\mathbf{x}_o)e^{2\pi e_l(\mathbf{x}_o)\Omega(\mathbf{x}_o, \mathbf{f})}$. This provides a local frequency description of component l at \mathbf{x}_o . The instantaneous frequency should be interpreted in terms of the local frequency of the oscillations, $|\phi'_l(\mathbf{x}_o)|$, and the orientation of these oscillations, $\mathbf{n}_l(\mathbf{x}_o)$. The sign of $\phi'_l(\mathbf{x}_o)$ is taken so that the orientation angle is restricted from $-\frac{\pi}{2}$ to $\frac{\pi}{2}$. Finally the local magnitude $a_l(\mathbf{x}_o)$ has the interpretation of local energy presence. If the image is actually a sum of several AM/FM/OM terms, *i.e.* the signal is multi-component, as is most often the case of many observed images, we will not be able to use this description directly, as we cannot separate out the L components. The problem with multi-component signals in one dimension is much documented [8], if not fully resolved, but generally calls for localised methods. We shall thus construct local monogenic descriptions of images. These descriptions extract well-behaved orientation, phase and amplitude functions locally, and also have excellent statistical properties.

VI. ORIENTATION & MONOGENIC WAVELETS

A. Definition

In one dimension the analytic Morse wavelets can be constructed from the even Morse wavelets, by adding i times the Hilbert transform of the original even function, to the even wavelet. The even Morse wavelets are invariant to sign changes, or direction, whilst the odd Morse wavelets, are naturally odd

functions. We construct a monogenic version of isotropic wavelets in two dimensions, based on the real isotropic Morse wavelets, using the Riesz transform. The monogenic wavelet transform locally defines a phase and an orientation for a real image at each spatial and spatial scale point, similarly to the monogenic signal. The monogenic wavelets are most easily represented as quaternion-valued functions defined for each n via

$$\psi_n^{(+)}(\mathbf{x}) = \psi_n^{(e)}(\mathbf{x}) + i\psi_n^{(1)}(\mathbf{x}) + j\psi_n^{(2)}(\mathbf{x}) = \psi_n^{(e)}(\mathbf{x}) + \psi_n^{(q)}(\mathbf{x}), \quad (33)$$

where the Fourier transform of the real part of the monogenic wavelet is given by (23) and the additional two real functions are defined in the Fourier domain as Riesz transforms of the isotropic wavelet function via

$$\Psi_{n,l,m}^{(s)}(\mathbf{f}) = -j \frac{A_{n;l,m} f_s}{\sqrt{\pi}} (2\pi f)^l e^{-(2\pi f)^m} L_n^{l,m} (2(2\pi f)^m), \quad s = 1, 2. \quad (34)$$

Note that we consider $\psi_n^{(q)}(\mathbf{x}) = i\psi_n^{(1)}(\mathbf{x}) + j\psi_n^{(2)}(\mathbf{x})$, as a single object, and this has the same norm as $\psi_n^{(e)}(\mathbf{x})$. In subsequent analysis we fix (l, m) , and henceforth suppress their value, for notational convenience. For the case $(l, m) = (8, 3)$ plots of the Riesz transforms in the x_1 direction of the isotropic wavelets $n = 0, 1$ are given in the spatial domain (see Figure 2) as well as the spatial frequency domain, where their modulus is plotted. Note that the real component is an isotropic wavelet (like the even wavelet in one dimension) and the two components are odd in the x_1 and x_2 direction respectively. We define the translated, rotated and dilated wavelet $\psi_{\xi,n}^{(+)}(\mathbf{x})$, as the appropriate sum of translating, rotating and dilating its real valued components. The continuous wavelet transform of an image $g(\cdot)$ with respect to either the components of, or with respect to the full quaternionic wavelet, is defined as $w_n^{(\cdot)}(\xi; g) = \int d^2\mathbf{x} g(\mathbf{x}) \psi_{\xi,n}^{(\cdot)*}(\mathbf{x})$. The associated scalogram is $S_n^{(\cdot)}(\xi; g) = |w_n^{(\cdot)}(\xi; g)|^2$. The wavelet transform of image $g(\cdot)$ is then given via either the spatial domain, or spatial frequency domain, in terms of $\zeta = [a, \theta, \mathbf{f}_b]^T$, where \mathbf{f}_b is the Fourier variable for \mathbf{b} via

$$w_n^{(+)}(\xi; g) = w_n^{(e)}(\xi; g) - iw_n^{(1)}(\xi; g) - jw_n^{(2)}(\xi; g), \quad (35)$$

$$W_n^{(+)}(\zeta; g) = [1 - \mathbf{k} \cos(\phi - \theta) + \sin(\phi - \theta)] W_n^{(e)}(\zeta; g). \quad (36)$$

Thus the filtering carried out in the Fourier domain, can be understood, by looking at the wavelet function in the Fourier domain:

$$\Psi_{\xi,n}^{(+)}(\mathbf{f}) = [1 - \mathbf{k} \cos(\phi - \theta) + \sin(\phi - \theta)] \Psi_{\xi,n}^{(e)}(\mathbf{f}), \quad (37)$$

with modulus

$$\left| \Psi_{\xi,n}^{(+)}(\mathbf{f}) \right|^2 = 2(1 + \sin(\phi - \theta)) \left| \Psi_{\xi,n}^{(e)}(\mathbf{f}) \right|^2. \quad (38)$$

Hence in terms of \mathbf{b} and a the monogenic wavelet is filtering the image identically to the isotropic real wavelet, whilst the term $\sin(\phi - \theta)$ is positioning the image, in orientation, in relation to the wavelet. This representation clarifies that the rotation by angle θ of the wavelet function, as repositioning the axis of analysis, by a rotation of θ . Note that the modulus of the real isotropic wavelet is invariant with respect to θ .

Finally consider the joint structure of the N wavelets. We obtain that (see Appendix A)

$$\begin{aligned} \langle \psi_{n_1}^{(e)}, \psi_{n_2}^{(e)} \rangle &= \delta_{n_1, n_2}, & \langle \psi_{n_1}^{(l)}, \psi_{n_2}^{(l)} \rangle &= \frac{1}{2} \delta_{n_1, n_2}, \\ \langle \psi_{n_1}^{(1)}, \psi_{n_2}^{(2)} \rangle &= 0, & \langle \psi_{n_1}^{(e)}, \psi_{n_2}^{(l)} \rangle &= 0, \quad l = 1, 2. \end{aligned} \quad (39)$$

The multiple Morse wavelets thus form an orthogonal system, and this will have implications for their usage when performing estimation of local characteristics of real images. The total energy of the image using the n th wavelet is given by

$$\begin{aligned} S_n^{(+)}(\boldsymbol{\xi}; g) &= S_n^{(e)}(\boldsymbol{\xi}; g) + S_n^{(1)}(\boldsymbol{\xi}; g) + S_n^{(2)}(\boldsymbol{\xi}; g) \\ &= S_n^{(e)}(\boldsymbol{\xi}; g) + S_n^{(q)}(\boldsymbol{\xi}; g). \end{aligned} \quad (40)$$

Also note that, as $\psi^{(e)}(\cdot)$ is radially symmetric,

$$\begin{aligned} w_n^{(1)}(\boldsymbol{\xi}; g) &= \cos(\theta)w_n^{(1)}(\boldsymbol{\xi}_0; g) + \sin(\theta)w_n^{(2)}(\boldsymbol{\xi}_0; g), \\ w_n^{(2)}(\boldsymbol{\xi}; g) &= -\sin(\theta)w_n^{(1)}(\boldsymbol{\xi}_0; g) + \cos(\theta)w_n^{(2)}(\boldsymbol{\xi}_0; g), \end{aligned} \quad (41)$$

where $\boldsymbol{\xi}_0 = (a, 0, \mathbf{b})$. Thus the wavelet transform needs only be calculated for one orientation, and can then be formed for any orientation by judicious recombination. We consider now the analysis of typical image features with the monogenic Morse wavelets.

VII. THE MONOGENIC WAVELET TRANSFORM OF DISCONTINUITIES

We consider both point and line discontinuities. The idealised version of a point discontinuity at \mathbf{x}_0 corresponds to: $g_{s,1}(\mathbf{x}) = a_1(\mathbf{x})\delta(\mathbf{x} - \mathbf{x}_0)$, where $a_1(\mathbf{x})$ is assumed to be a well-behaved function at point $\mathbf{x} = \mathbf{x}_0$. This singularity is characterised by \mathbf{x}_0 , its location, and $a_1(\mathbf{x}_0)$, the amplitude of the location. The wavelet transform of this object is $w^{(+)}(\boldsymbol{\xi}; g) = a_1(\mathbf{x}_0)\psi_{\boldsymbol{\xi}}^{(+)*}(\mathbf{r}_{-\theta}(\mathbf{x}_0 - \mathbf{b})/a)/a$. This is clearly maximum near $\mathbf{b} = \mathbf{x}_0$ where it has a modulus square of $a_1^2(\mathbf{x}_0) \left| \psi_{\boldsymbol{\xi}}^{(+)}(\mathbf{0}) \right|^2 / a^2$, and hence point singularities can be located by finding maxima in \mathbf{b} . Furthermore $|w^{(+)}(\boldsymbol{\xi}; g)|^2$ has no dependence on θ , and as the magnitude of the wavelet at the origin is known, $a_1(\cdot)$ can be determined. A one-dimensional singularity is modelled as

$$g_{s,2}(\mathbf{x}) = a_2(x_1)\delta(\cos(\theta_2)x_1 + \sin(\theta_2)x_2 - c). \quad (42)$$

The line $x_2 = c$ ($\theta_2 = \pi/2$) modulated by the value of $a_2(x_1)$ is permitted, however we do not permit the line $x_1 = c$ ($\theta_2 = 0$), as this would lead to an image of infinite energy. We will anticipate a further constraint on θ_2 , that is $-\frac{\pi}{4} < \theta_2 \leq \frac{3\pi}{4}$, which we will explain at the end of this section. Assume that $a_2(x_1)$ is a symmetric function around a maximum at $x_1 = x_{1,\max}$. We characterise the structure of $g_{s,2}(\cdot)$, using the wavelet transform. The wavelet transform using the isotropic wavelet only, noting that $\psi_n^{(e)}(\mathbf{x}) = \psi_{n,r}^{(e)}(x)$, (where $\psi_{n,r}^{(e)}(x) \approx 0 \forall x > x_r$) is

$w_n^{(e)}(\boldsymbol{\xi}, g_{s,2}) = \int_{-\infty}^{\infty} a_2(x_1)/a\psi_{n,r}^{(e)}\left(a\sqrt{(x_1 - b_1)^2 + (c \csc(\theta_2) - \cot(\theta_2)x_1 - b_2)^2}\right) dx_1$. This will be large for values of \mathbf{b} such that $\sqrt{(x_{1,\max} - b_1)^2 + (c \csc(\theta_2) - \cot(\theta_2)x_{1,\max} - b_2)^2} < x_r/a$. Similar results hold for $w_n^{(e)}(\boldsymbol{\xi}, g_{s,2})$, as the Riesz transforms roughly have the same spatial support as the original wavelet. Hence we identify the location of the singularity for any fixed value a as $\mathbf{b} = (x_{1,\max}, c \csc(\theta_2) - \cot(\theta_2)x_{1,\max})$, as maxima in the modulus of the wavelet transform using the monogenic wavelet. The orientation θ_2 will thus visually be apparent from the \mathbf{b} plane but can also be characterised at a *fixed* point $\boldsymbol{\xi}$. The Fourier transform of (42) is

$$G_{s,2}(\mathbf{f}) = \frac{A_2(f_1 - \cot(\theta_2)f_2)}{|\sin(\theta_2)|} e^{-j2\pi(f_1 \cos(\theta_2) + f_2 \sin(\theta_2))c} e^{-j2\pi(-\sin(\theta_2)f_1 + \cos(\theta_2)f_2)c \cot(\theta_2)}$$

where $A_2(\cdot)$ is the Fourier Transform of $a_2(\cdot)$. The wavelet transform of this image is $W_n^{(l)}(\boldsymbol{\zeta}_0; g_{s,2}) = j \frac{f_{b,1}}{f_b} a \Psi_n^{(e)}(af_b) G_{s,2}(\mathbf{f})$, where $\boldsymbol{\zeta}_0 = [a, 0, \mathbf{f}_b]$. Thus we find that the Fourier transform of the rotated wavelet is given by $W_n^{(1)}(\boldsymbol{\zeta}; g_{s,2}) = j \frac{\cos(\theta)f_{b,1} + \sin(\theta)f_{b,2}}{f_b} a \Psi_n^{(e)}(af_b) G_{s,2}(\mathbf{f})$, with the obvious extension for $W_n^{(2)}(\boldsymbol{\zeta}; g_{s,2})$. Now we choose to evaluate the wavelet transform with $\theta_2 = \theta$, and define $\boldsymbol{\xi}_2 = [a, \theta, \mathbf{b}]$.

$$\begin{aligned} w_n^{(1)}(\boldsymbol{\xi}_2; g_{s,2}) &= \frac{1}{|\sin(\theta)|} \int_{-\infty}^{\infty} j \frac{f_{\theta,b,1}}{f_{\theta,b}} e^{j2\pi f_{\theta,b,1}[(\mathbf{r}_{-\theta}\mathbf{b})_1 - c]} \\ &\quad \int_{-\infty}^{\infty} a \Psi_n^{(e)}(af_{\theta,b}) e^{j2\pi f_{\theta,b,2}[(\mathbf{r}_{-\theta}\mathbf{b})_2 - c \cot(\theta)]} A_2\left(-\frac{f_{\theta,b,2}}{\sin(\theta)}\right) df_{\theta,b,2} df_{\theta,b,1} \\ &= \frac{1}{|\sin(\theta)|} \int_{-\infty}^{\infty} j \frac{f_{\theta,b,1}}{f_{\theta,b}} e^{j2\pi f_{\theta,b,1}[(\mathbf{r}_{-\theta}\mathbf{b})_1 - c]} \tilde{A}_2(f_{\theta,b,1}^2; \boldsymbol{\xi}_2, c) df_{\theta,b,1}, \end{aligned}$$

where the last equation defines $\tilde{A}_2(f_{\theta,b,1}^2; \boldsymbol{\xi}_2, c)$, as an *even* function of $f_{\theta,b,1}$, and $\mathbf{f}_{\theta,b} = [f_{\theta,b,1}, f_{\theta,b,2}] = \mathbf{r}_{-\theta}\mathbf{f}_b$. Note that for fixed values of a and $\theta = \theta_2$ we can find a value of \mathbf{b} such that $(\mathbf{r}_{-\theta}\mathbf{b})_1 = c$, denoted \mathbf{b}_2 . When $\boldsymbol{\xi} = \boldsymbol{\xi}'_2 = [a, \theta, \mathbf{b}_2]$ then $\sin\{(2\pi f_{\theta,b,1})[(\mathbf{r}_{-\theta}\mathbf{b})_1 - c]\}$ vanishes identically for all $f_{\theta,b,1}$. Hence $w_n^{(1)}(\boldsymbol{\xi}'_2; g_{s,2}) = 0$, whilst from equation (41) we find that the energy of the wavelet transform with $\psi^{(g)}(\cdot)$ is conserved under rotations. Thus $|w^{(2)}(\boldsymbol{\xi}; g)|$ is maximum at $\theta = \theta_2$, and $\mathbf{b} = \mathbf{b}_2$. With the correct choice of rotation θ we find that we can retrieve the angle θ_2 via maximising the energy of $w_n^{(2)}(\boldsymbol{\xi}; g_{s,2})$ and minimising the energy of $w_n^{(1)}(\boldsymbol{\xi}; g_{s,2})$. If the magnitudes of the two wavelet transforms at $\boldsymbol{\xi} = \boldsymbol{\xi}_0$

are equal then $\theta = 3\pi/4$. Otherwise we take a value of θ that maximises

$$\begin{aligned} w_n^{(2)2}(\boldsymbol{\xi}; g_{s,2}) - w_n^{(1)2}(\boldsymbol{\xi}; g_{s,2}) &= \cos(2\theta) \left(-w_n^{(1)2}(\boldsymbol{\xi}_0; g_{s,2}) + w_n^{(2)2}(\boldsymbol{\xi}_0; g_{s,2}) \right) \\ &\quad - 2 \sin(2\theta) w_n^{(1)}(\boldsymbol{\xi}_0; g_{s,2}) w_n^{(2)}(\boldsymbol{\xi}_0; g_{s,2}). \end{aligned} \quad (43)$$

This has a stationary point at

$$\theta_{\max,n} = \frac{1}{2} \tan^{-1} \left(\frac{2w_n^{(1)}(\boldsymbol{\xi}_0; g_{s,2})w_n^{(2)}(\boldsymbol{\xi}_0; g_{s,2})}{w_n^{(1)2}(\boldsymbol{\xi}_0; g_{s,2}) - w_n^{(2)2}(\boldsymbol{\xi}_0; g_{s,2})} \right), \quad (44)$$

which corresponds to a maximum by choosing the appropriate solution. Note that if $\left| w_n^{(2)}(\boldsymbol{\xi}_0; g_{s,2}) \right| > \left| w_n^{(1)}(\boldsymbol{\xi}_0; g_{s,2}) \right|$ we choose the solution $-\frac{\pi}{4} < \theta < \frac{\pi}{4}$ that corresponds to a maximum whilst if $\left| w_n^{(2)}(\boldsymbol{\xi}_0; g_{s,2}) \right| < \left| w_n^{(1)}(\boldsymbol{\xi}_0; g_{s,2}) \right|$ we take $\frac{\pi}{4} < \theta \leq \frac{\pi}{2}$, or $-\frac{\pi}{2} < \theta < -\frac{\pi}{4}$. Thus at any fixed point $\boldsymbol{\xi}$ we can find the orientation that would result from a line-discontinuity passing through \mathbf{b} , by utilising the above equation, and this characterises local orientational structure. Note also that at $\boldsymbol{\xi} = \boldsymbol{\xi}'_2$ as this evaluates the wavelet transform at values of \mathbf{b} corresponding to the discontinuity, $\left| w_n^{(+)}(\boldsymbol{\xi}'_2; g_{s,2}) \right|^2$ will be large. A plot of parameter $\theta_{\max,n}$ should be combined with a plot of $\left| w_n^{(+)}(\boldsymbol{\xi}'_2; g_{s,2}) \right|^2$ to verify that local rapid variation corresponding to an edge is present.

VIII. THE MONOGENIC WAVELET TRANSFORM OF AM/FM/OM IMAGES

Consider analysis of images of the form given by equation (29). For more general classes of images, i.e. such as images that are constrained to be positive we may add a constant term to the model, but as noted by [14], the wavelet transform is a zero-mean filter, and so this makes no difference to the subsequent analysis. We then find that

$$\begin{aligned} w_n^{(e)}(\boldsymbol{\xi}; c_l) &= \frac{1}{2} \int \int a_l(\mathbf{b}) \left[e^{2j\pi(\phi_l(\mathbf{b}) + \phi'_l(\mathbf{b})\mathbf{n}_l(\mathbf{b}) \cdot (\mathbf{x} - \mathbf{b}))} + e^{-2j\pi(\phi_l(\mathbf{b}) + \phi'_l(\mathbf{b})\mathbf{n}_l(\mathbf{b}) \cdot (\mathbf{x} - \mathbf{b}))} \right] \psi_{\boldsymbol{\xi},n}^{(e)*}(\mathbf{x}) d^2\mathbf{x} \\ &= a_l(\mathbf{b}) \cos[2\pi\phi_l(\mathbf{b})] a\Psi_n^{(e)}(a\phi'_l(\mathbf{b})), \\ w_n^{(m)}(\boldsymbol{\xi}_0; c_l) &= \frac{1}{2} \int \int a_l(\mathbf{b}) \left[e^{2j\pi(\phi_l(\mathbf{b}) + \phi'_l(\mathbf{b})\mathbf{n}_l(\mathbf{b}) \cdot (\mathbf{x} - \mathbf{b}))} + e^{-2j\pi(\phi_l(\mathbf{b}) + \phi'_l(\mathbf{b})\mathbf{n}_l(\mathbf{b}) \cdot (\mathbf{x} - \mathbf{b}))} \right] \psi_{\boldsymbol{\xi}_0,n}^{(m)*}(\mathbf{x}) d^2\mathbf{x} \\ &= \frac{1}{2} a_l(\mathbf{b}) \left[e^{2j\pi\phi_l(\mathbf{b})} a\Psi_n^{(m)*}(a\phi'_l(\mathbf{b})\mathbf{n}_l(\mathbf{b})) + e^{-2j\pi\phi_l(\mathbf{b})} a\Psi_n^{(m)*}(-a\phi'_l(\mathbf{b})\mathbf{n}_l(\mathbf{b})) \right], \quad m = 1, 2. \end{aligned}$$

Hence it follows from equation (41) that $w^{(+)}(\boldsymbol{\xi}; c_l) = a_l(\mathbf{b}) a\Psi_n^{(e)}(a\phi'_l(\mathbf{b})) e^{2\pi\mathbf{e}_{\nu_l} \cdot \phi_l(\mathbf{b})}$, with $\mathbf{e}_{\nu_l} = \mathbf{i} \cos(\eta_l(\mathbf{b}) - \theta) + \mathbf{j} \sin(\eta_l(\mathbf{b}) - \theta)$. This is the localised analogue of equation (31). For multi-component images, we may be able to separate the dominant component out, similarly to ridge analysis based on complex wavelets [14]; this requiring the assumption $a_l(\mathbf{b}) a\Psi_n^{(e)}(a\phi'_l(\mathbf{b})) \gg a_m(\mathbf{b}) a\Psi_n^{(e)}(a\phi'_l(\mathbf{b})) \forall l \neq$

m , at all $\boldsymbol{\xi}$ considered. Furthermore, the modulus of the wavelet transform is

$$\left|w^{(+)}(\boldsymbol{\xi}; c_l)\right|^2 = a_l^2(\mathbf{b})a^2\Psi_n^{(e)2}(a\phi_l'(\mathbf{b})), \quad (45)$$

and hence the wavelet transform of $c_l(\cdot)$ is locally maximal on the curve given by

$\mathcal{R}(a, \theta, \mathbf{b}) = \{(a, \mathbf{b}) : a\phi_l'(\mathbf{b}) = f_{\max}^{(n)}\}$, where $f_{\max}^{(n)}$ is given by (24). This defines the monogenic wavelet ridges [14] of an AM/FM/OM images. At any point on this ridge, the local orientation may be computed. Ridge analysis is based on the fact that not all information of the redundant wavelet transform representation needs to be considered to characterise the image: only the ridge itself. As the ridge definition does not depend on the angle θ , we need not carry out the transform for all these values; a computational advantage to using directional wavelets. On the ridge we characterise the oscillatory components locally as

$$\nu_l(\mathbf{b}) = \tan^{-1}\left(\frac{w^{(2)}(\boldsymbol{\xi}; c_l)}{w^{(1)}(\boldsymbol{\xi}; c_l)}\right) = \eta_l(\mathbf{b}) - \theta, \quad (46)$$

$$\phi_l(\mathbf{b}) = \frac{1}{2\pi} \tan^{-1}\left(\frac{\text{sgn}(w^{(2)}(\boldsymbol{\xi}; c_l)) \sqrt{w^{(1)2}(\boldsymbol{\xi}; c_l) + w^{(2)2}(\boldsymbol{\xi}; c_l)}}{w^{(e)}(\boldsymbol{\xi}; c_l)}\right), \quad (47)$$

$$a_l^2(\mathbf{b}) = \frac{|w^{(+)}(\boldsymbol{\xi}; c_l)|^2}{a^2\Psi_n^{(e)2}(a\phi_l'(\mathbf{b}))}. \quad (48)$$

We have constrained $-\frac{\pi}{2} \leq \nu_l \leq \frac{\pi}{2}$ and $-\frac{1}{2} \leq \phi \leq \frac{1}{2}$ by the choice of sign for the $\tan^{-1}(\cdot)$.

IX. DIGITAL IMPLEMENTATION

To preserve the exact monogenic structure we implement the wavelet transform from the Fourier domain, calculating the IDFT, thus making the algorithm of order $O(N_1 N_2 \log(N_1) \log(N_2))$. We consider the maximum and minimum scales that can be resolved - the range of the angle $\theta \in (0, 2\pi)$ and $\mathbf{b} \in (0, N_1\Delta_1) \times (0, N_2\Delta_2)$. As the real two-dimensional even wavelet $\Psi_n^{(e)}(\cdot)$ is built from a real one-dimensional wavelet corresponding to a band-pass filter, there exist frequencies $f_1^{(n)}$ and $f_2^{(n)}$ such that

$$\Psi_n^{(e)}(f) \approx 0 \quad \forall f : |f| \notin (f_1^{(k)}, f_2^{(n)}). \quad (49)$$

Note that the DFT of observed image $g(\cdot, \cdot)$ is periodic by construction, and that the standard assumption corresponds to $G(f_1, f_2) = 0$ for all frequencies not in the Nyquist band. Thus to perform the implementation we consider only scales a such that $\Psi_n^{(e)}\left(a\sqrt{f_1^2 + f_2^2}\right) \approx 0 \quad \forall \mathbf{f} : f_1 \geq 1/(2\Delta_1), f_2 \geq 1/(2\Delta_2)$. This necessitates $a \geq a_{\min} = 2f_2^{(n)} \frac{\Delta_1\Delta_2}{\sqrt{\Delta_1^2 + \Delta_2^2}}$. As a increases in magnitude, the wavelet becomes more peaked in the frequency domain, and to ensure the wavelet covers at least M frequency points we constrain $a \leq a_{\max} = \frac{1}{M} \min(N_1\Delta_1, N_2\Delta_2) \left[f_2^{(n)} - f_1^{(n)}\right]$.

X. STATISTICAL PROPERTIES

Consider estimation of features present in an image immersed in white noise where the image is collected in a regular grid consisting of $x_1 = s_1\Delta_1$, $s_1 = 0, \dots, N_1 - 1$ and $x_2 = s_2\Delta_2$, $s_2 = 0, \dots, N_2 - 1$. We model the observed image $y(x_1, x_2)$ as $y(x_1, x_2) = g(x_1, x_2) + \epsilon_{s_1, s_2}$. The noise $\{\epsilon_{s_1, s_2}\}$ is modelled as isotropically Gaussian and white. It is assumed that $E(\epsilon_{s_1, s_2}) = 0$, and $E(\epsilon_{s_1, s_2}, \epsilon_{u_1, u_2}) = \delta_{s_1, u_1} \delta_{s_2, u_2} \sigma_\epsilon^2$. The wavelet transform of the noise will also be Gaussian, as it corresponds to a sum of jointly normal variables. To give the distribution of the wavelet transform, we calculate its first and second order structure at a fixed ξ . The wavelet transform is a linear operation and $w_n^{(\cdot)}(\xi; y) = w_n^{(\cdot)}(\xi; g) + w_n^{(\cdot)}(\xi; \epsilon)$. It follows that $E(w_n^{(\cdot)}(\xi; y)) = w_n^{(\cdot)}(\xi; g)$, and we can determine the second order structure of the estimators from the distribution of the noise.

We recast the full wavelet transform of the noise as a vector with real valued entries, $\mathbf{w}_n(\xi; \epsilon) = [w_n^{(e)}(\xi; \epsilon) \ w_n^{(1)}(\xi; \epsilon) \ w_n^{(2)}(\xi; \epsilon)]^T$, $n = 0, \dots, N - 1$. In Appendix B, we find with the additional assumption of

$$\min\left(\frac{1}{2\Delta_1}, \frac{1}{2\Delta_2}\right) > \max_{n=0, \dots, N-1} f_{\max}^{(n)}, \quad (50)$$

that

$$\mathbf{w}_n(\xi; \epsilon) \stackrel{d}{=} \mathcal{N}_3(\mathbf{0}_3, \sigma_\epsilon^2 \mathbf{V}), \quad \mathbf{V} = \begin{pmatrix} 1 & 0 & 0 \\ 0 & \frac{1}{2} & 0 \\ 0 & 0 & \frac{1}{2} \end{pmatrix}. \quad (51)$$

We perform estimation using the multiple orthogonal wavelets. Any estimator of local signal properties needs to be smoothed, or averaged to obtain a low variance. The wavelet transform using any of the specified wavelet functions averages the data across a window in space and spatial frequency, where the width of the region depends on the wavelet chosen, and in our case is characterised by the radial Morse region \mathcal{D} , and the parameters $(\beta = l + \frac{1}{2}, \gamma = m)$. Thomson [1] suggested forming estimates of local properties by averaging local energy estimates using several orthogonal wavelets/functions. This usage explicitly reduces the variability of the estimates with a clearly specified averaging region – \mathcal{D} . Coherent behaviour over \mathcal{D} is re-enforced across wavelet estimates, but the noisy uncorrelated behaviour should cancel. The bias inherent in the averaging is characterised by the eigenvalues square of the localisation operator. In Appendix B we show that $E(w_{n_1}^{(l_1)}(\xi; \epsilon) w_{n_2}^{(l_2)}(\xi; \epsilon)) = \sigma_\epsilon^2 V^{l_1 l_2} \delta_{n_1, n_2}$, and thus $\mathbf{w}_{n_1}(\xi; \epsilon)$ is uncorrelated with $\mathbf{w}_{n_2}(\xi; \epsilon)$ unless $n_1 = n_2$, that combined with the assumption of Gaussian errors corresponds to independence. We define averages of the wavelet transform and the scalogram that will

be used as a basis for calculating estimators of other quantities as

$$\overline{w}^{(l)}(\boldsymbol{\xi}; \cdot) = \frac{1}{N} \sum_{n=0}^{N-1} w_n^{(l)}(\boldsymbol{\xi}; \cdot) \quad \overline{S}^{(l)}(\boldsymbol{\xi}; \cdot) = \frac{1}{N} \sum_{n=0}^{N-1} S_n^{(l)}(\boldsymbol{\xi}; \cdot), \quad (52)$$

with $l = e, 1, 2, +$, and finally as a measure of covariation we define for $l_1, l_2 = e, 1, 2, +$, and images $g_1(\cdot), g_2(\cdot)$, $\overline{C}^{(l_1, l_2)}(\boldsymbol{\xi}; g_1(\cdot), g_2(\cdot)) = \frac{1}{N} \sum_{n=0}^{N-1} w_n^{(l_1)}(\boldsymbol{\xi}; g_1) w_n^{(l_2)*}(\boldsymbol{\xi}; g_2)$. We define the estimators $\widehat{w}^{(l)}(\boldsymbol{\xi}; g) = \overline{w}^{(l)}(\boldsymbol{\xi}; y)$ and $\widehat{S}^{(l)}(\boldsymbol{\xi}; g) = \overline{S}^{(l)}(\boldsymbol{\xi}; y)$, for $l = e, 1, 2, +$, as well as $\widehat{w}^{(l_1)w^{(l_2)}}(\boldsymbol{\xi}; g_1) = \overline{C}^{(l_1, l_2)}(\boldsymbol{\xi}; g_1(\cdot), g_1(\cdot))$. The Gaussian assumptions on ϵ then give $\overline{w}(\boldsymbol{\xi}; \epsilon) = [\overline{w}^{(e)}(\boldsymbol{\xi}; \epsilon), \overline{w}^{(1)}(\boldsymbol{\xi}; \epsilon), \overline{w}^{(2)}(\boldsymbol{\xi}; \epsilon)] \stackrel{d}{=} \mathcal{N}(\mathbf{0}_3, \overline{\sigma}_\epsilon^2 \mathbf{V})$, where $\overline{\sigma}_\epsilon^2 = \sigma_\epsilon^2/N$. For most quantities we would intuitively expect to see a reduction of $1/N$ in their variances. When estimating the energy of the image at point $\boldsymbol{\xi}$ we consider

$$\widehat{S}^{(+)}(\boldsymbol{\xi}; g) = \frac{1}{N} \sum_{n=0}^{N-1} S_n^{(+)}(\boldsymbol{\xi}; y) \quad (53)$$

$$= \overline{S}^{(+)}(\boldsymbol{\xi}; g) + \overline{S}^{(+)}(\boldsymbol{\xi}; \epsilon) + \frac{2}{N} \sum_{n=0}^{N-1} \left[w_n^{(e)}(\boldsymbol{\xi}; g) w_n^{(e)}(\boldsymbol{\xi}; \epsilon) \right. \quad (54)$$

$$\left. + w_n^{(1)}(\boldsymbol{\xi}; g) w_n^{(1)}(\boldsymbol{\xi}; \epsilon) + w_n^{(2)}(\boldsymbol{\xi}; g) w_n^{(2)}(\boldsymbol{\xi}; \epsilon) \right] \quad (55)$$

Up to order $\overline{\sigma}_\epsilon^2$, we find, with the additional assumption of the localised behaviour of $g(\cdot)$ coherent across the n wavelets,

$$\widehat{S}^{(+)}(\boldsymbol{\xi}; g) \stackrel{d}{=} \mathcal{N} \left(\overline{S}^{(+)}(\boldsymbol{\xi}; g), 4 \frac{\sigma_\epsilon^2}{N} \left[\overline{S}^{(e)}(\boldsymbol{\xi}; g) + \frac{1}{2} \left(\overline{S}^{(1)}(\boldsymbol{\xi}; g) + \overline{S}^{(2)}(\boldsymbol{\xi}; g) \right) \right] \right). \quad (56)$$

Hence the variance of the energy estimate decreases $O\left(\frac{1}{N}\right)$.

A. Distribution of Estimators

We estimate the orientation of the line discontinuity in section VII by maximising the difference between the energy of the second and first components. Each wavelet indexed by n satisfies equation (44) and thus writing the equations in terms of $\tan(\theta_{\max, n}) = \theta_2$, we may sum over the equations to find that

$$\theta_2 = \frac{1}{2} \tan^{-1} \left(\frac{2 \overline{C}^{(1, 2)}(\boldsymbol{\xi}; g_{s, 2}, g_{s, 2})}{\overline{S}^{(1)}(\boldsymbol{\xi}_0; g_{s, 2}) - \overline{S}^{(2)}(\boldsymbol{\xi}_0; g_{s, 2})} \right).$$

We form estimate

$$\widehat{\theta}_{\max}(g_{s, 2}) = \frac{1}{2} \tan^{-1} \left(\frac{2 \widehat{w}^{(1)w^{(2)}}(\boldsymbol{\xi}; g_{s, 2})}{\widehat{S}^{(1)}(\boldsymbol{\xi}_0; g_{s, 2}) - \widehat{S}^{(2)}(\boldsymbol{\xi}_0; g_{s, 2})} \right).$$

Let $w_n^{(l)}(\boldsymbol{\xi}; \epsilon) = \sigma_\epsilon w_{n, \epsilon}^{(l)}$, which entails that $\overline{w}^{(l)}(\boldsymbol{\xi}; \epsilon) = \sigma_\epsilon \overline{w}_\epsilon^{(l)}$ for $l = e, 1, 2, +$, and expand the above expression $\widehat{\theta}_{\max}(g_{s, 2}) = \theta_2 + \sigma_\epsilon \delta\theta_2 + O(\sigma_\epsilon^2)$. Note that $E(\delta\theta_2) = 0$ making the estimator up to order

σ_ϵ^2 unbiased, and the estimator has variance

$$\text{Var} \left[\hat{\theta}_{\max}(g_{s,2}) \right] = \frac{\sigma_\epsilon^2}{N} \frac{1}{2} \frac{\overline{S}^{(1)}(g_{s,2}) + \overline{S}^{(2)}(g_{s,2})}{\left[\overline{S}^{(1)}(g_{s,2}) - \overline{S}^{(2)}(g_{s,2}) \right]^2 + 4 \left[\overline{C}^{(1,2)}(g_{s,2}, g_{s,2}) \right]^2} + O(\sigma_\epsilon^3). \quad (57)$$

Thus, using multiple wavelets leads to a variance reduction.

For AM/FM/OM signals we define the estimator for the orientation angle of the unit quaternion as

$$\hat{\nu}_l(\boldsymbol{\xi}; c_l) = \bar{\nu}_l(\boldsymbol{\xi}; y_l) = \tan^{-1} \left[\frac{\widehat{w}^{(2)}(\boldsymbol{\xi}; c_l)}{\widehat{w}^{(1)}(\boldsymbol{\xi}; c_l)} \right], \quad (58)$$

that up to order σ_ϵ^2 is

$$\hat{\nu}_l(\boldsymbol{\xi}; c_l) = \nu_l(\boldsymbol{\xi}; c_l) + \sigma_\epsilon \frac{\overline{w}^{(1)}(\boldsymbol{\xi}; c_l) \overline{w}_\epsilon^{(2)} - \overline{w}^{(2)}(\boldsymbol{\xi}; c_l) \overline{w}_\epsilon^{(1)}}{\overline{S}^{(1)}(\boldsymbol{\xi}; c_l) + \overline{S}^{(2)}(\boldsymbol{\xi}; c_l)} + O(\sigma_\epsilon^2) \quad (59)$$

as $\overline{w}^{(1)}(\boldsymbol{\xi}_0; c_l) = a_l(\mathbf{b}) \sin(2\pi\phi_l(\mathbf{b})) \cos(\nu_l) \frac{a}{N} \sum \Psi_{n_1}(a|\nabla\phi_l(\mathbf{b})|)$ and a similar results holds for the second component we have $\tan(\nu_l) = \frac{\overline{w}^{(1)}(\boldsymbol{\xi}; c_l)}{\overline{w}^{(2)}(\boldsymbol{\xi}; c_l)}$. As the wavelet transform of the noise has expectation zero the estimator is unbiased and it has variance

$$\text{Var} [\hat{\nu}_l(\boldsymbol{\xi}; c_l)] = \frac{\sigma_\epsilon^2}{2N} \frac{\overline{w}^{(1)2}(\boldsymbol{\xi}; c_l) + \overline{w}^{(2)2}(\boldsymbol{\xi}; c_l)}{\left[\overline{S}^{(1)}(\boldsymbol{\xi}; c_l) + \overline{S}^{(2)}(\boldsymbol{\xi}; c_l) \right]^2} + O(\sigma_\epsilon^3) \quad (60)$$

$$= \frac{\sigma_\epsilon^2}{2N^2} \frac{(\sum \Psi_{n_1}(a|\nabla\phi_l(\mathbf{b})|))^2}{\sum \Psi_{n_1}^2(a|\nabla\phi_l(\mathbf{b})|)} \approx \frac{\sigma_\epsilon^2}{2N}. \quad (61)$$

Using multiple wavelets leads to variance reduction. To estimate the phase we only use a single wavelet, the $n = 0$. Due to the orthogonality relations, the wavelet filters in the Fourier domain cannot be strictly positive for all frequencies, and thus for $n > 0$ there are induced variations in the phase estimate whenever the wavelet filter changes sign. The Morse wavelet estimate of the phase still profits from the wavelet's good radial localisation.

$$\begin{aligned} \hat{\phi}_l(\boldsymbol{\xi}; c_l) &= \phi_{0,l}(\boldsymbol{\xi}; c_l) + O(\sigma_\epsilon^2) \\ &+ \frac{\sigma_\epsilon}{2\pi} \left[\frac{-\left(S_0^{(1)}(\boldsymbol{\xi}; c_l) + S_0^{(2)}(\boldsymbol{\xi}; c_l) \right) w_{\epsilon,0}^{(e)} + w_0^{(e)}(\boldsymbol{\xi}; c_l) \left[w_{\epsilon,0}^{(1)} w_0^{(1)}(\boldsymbol{\xi}; c_l) + w_{\epsilon,0}^{(2)} w_0^{(2)}(\boldsymbol{\xi}; c_l) \right]}{S_0^{(+)}(\boldsymbol{\xi}; c_l) \sqrt{S_0^{(1)}(\boldsymbol{\xi}; c_l) + S_0^{(2)}(\boldsymbol{\xi}; c_l)}} \right]. \end{aligned} \quad (62)$$

As the expected value of the wavelet transform of noise is zero, the estimator is thus unbiased, and the variance of the phase estimator is

$$\text{Var} \left[\hat{\phi}_l(\boldsymbol{\xi}; c_l) \right] = \frac{\sigma_\epsilon^2}{S_0^{(+)}(\boldsymbol{\xi}; c_l)} \frac{S_0^{(+)}(\boldsymbol{\xi}; c_l) - \frac{1}{2} S_0^{(e)}(\boldsymbol{\xi}; c_l)}{(2\pi)^2 S_0^{(+)}(\boldsymbol{\xi}; c_l)} = \frac{\sigma_\epsilon^2}{(2\pi)^2 S_0^{(+)}(\boldsymbol{\xi}; c_l)} \left[1 - \frac{1}{2} \cos^2(2\pi\phi_l(\mathbf{b})) \right]. \quad (63)$$

When considering larger scales, the wavelets are averaging across a lot of sample points, and the variance of the phase estimate decreases. The amplitude is estimated as $\hat{a}_l^2(\mathbf{b}) = \frac{\widehat{S}^{(+)}(\boldsymbol{\xi}; c_l)}{a^2 \Psi^{(e)2}(a\widehat{\phi}_l'(\mathbf{b}))}$.

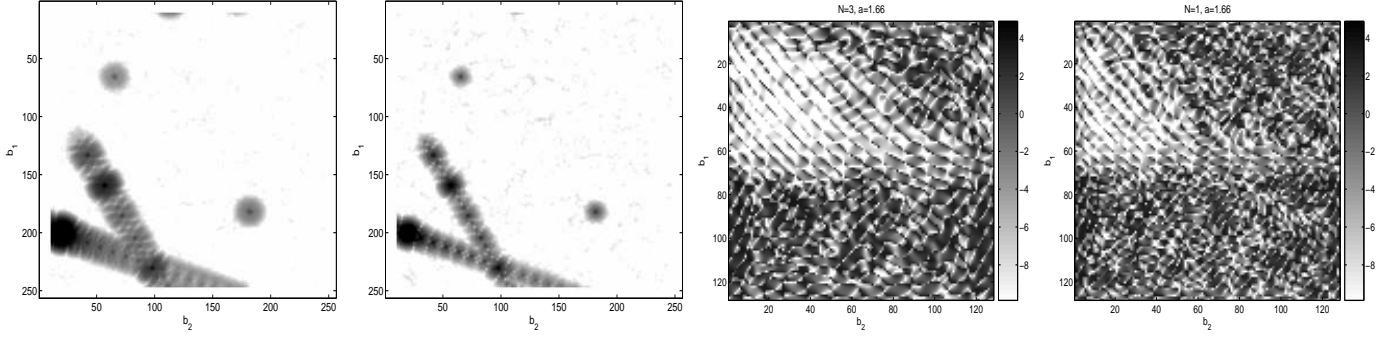


Fig. 3. The local energy of signal 1 on a dB scale using three wavelets (far left), or one wavelet (second from left), $a = 1.4$. The deviation of the estimated orientation from the true orientation at scale $a = 1.66$ using dB scale, using three wavelets (second from right) and one wavelet (far right). For the region where the signal has presence at those spatial and scale points, the estimate using three wavelets is less noisy.

XI. EXAMPLES

Consider a collection of singularities observed in noise: $g_1(\mathbf{x}) = \sum g_{2j}(\mathbf{x}) + \sigma_1 \epsilon_{\mathbf{x}}$ where $g_{11}(\mathbf{x}) = \frac{10}{\|\mathbf{x} - [\frac{1}{4}N_1 + \frac{1}{2}, \frac{1}{4}N_1 + \frac{1}{2}]^T\|}$, $g_{12}(\mathbf{x}) = \frac{15}{\|\mathbf{x} - [\frac{45}{64}N_1 + \frac{1}{2}, \frac{45}{64}N_1 + \frac{1}{2}]^T\|}$, $g_{13}(\mathbf{x}) = |x_1 \cos(\pi/3) - x_2 \sin(\pi/3) - \frac{15}{128}N_1 + \frac{1}{2}|^{-1}$, $g_{14}(\mathbf{x}) = |x_1 \cos(\pi/9) - x_2 \sin(\pi/9) - \frac{45}{64}N_1 + \frac{1}{2}|^{-1}$, and we take $\sigma_1 = 0.2$. The first two singularities of this signal are point singularities and the latter two are line singularities. See Figure 3 for a plot of the scalogram of the observed image at scale $a = 1.4$, corresponding to radial frequencies of 0.17. It can be clearly made out that the averaged estimate of the local energy is a great deal more robust to the noise. Signal 2 is a multi component AM/FM/OM signal given by $g_2(\mathbf{x}) = g_{21}(\mathbf{x}) + g_{22}(\mathbf{x}) + \sigma_2^2 \epsilon_{\mathbf{x}}$, where $g_{21}(\mathbf{x}) = 1.2I(x_1 < N_1/2) \cos\left(2\pi \times 0.087\left(\frac{t_2^2}{2N_1} + t_2\right)\right)$, $t_l = x_1 \cos(\eta_l) + x_2 \sin(\eta_l)$, $l = 1, 2$, $\eta_1 = -\frac{\pi}{4} + \frac{x_1 + x_2 - 155}{10N_1}$, $g_{22}(\mathbf{x}) = 0.8 \cos\left(0.05\pi\left(\frac{t_2^2}{10N_1} + t_2\right)\right)$, $\eta_2 = \frac{\pi}{5}$, and $N_1 = N_2 = 128$. We consider estimating its orientation at a scale where the more rapid sinusoid is present near the left-hand side at those frequencies, and find that our orientation estimate is substantively less noise when using multiple wavelets, as is confirmed by Figure 3. Clearly using the multiple wavelets is substantively decreasing the variability of the estimator.

XII. CONCLUSIONS

We show that the multiple monogenic Morse wavelets hold great potential for digital image processing and analysis. The monogenic Morse wavelets are the natural two-dimensional extension of the analytic Morse wavelets, and are the eigenfunctions of a two-dimensional, nonseparable, localisation operator. They form an orthogonal system, where the orthogonality establishes the statistical properties of Gaussian

noise. By averaging across wavelets, estimators of local properties of the signal achieve reduced variability. The monogenic properties of the wavelets form a natural framework for determining local phase and orientation properties. This framework explicitly parameterises the local orientation of any variational structure via a unit quaternion, and the localised analysis considers radial structures, thus using the natural metric of Cartesian distances in the spatial domain.

ACKNOWLEDGMENTS

SO & GM would like to thank Dr Frederik Simons for valuable discussions and SO would like to thank Professor Andrew Walden for introducing her to this research area. GM would like to acknowledge the EPSRC (UK) for their financial support.

REFERENCES

- [1] D. Thomson, "Spectrum Estimation and Harmonic Analysis," *Proc. IEEE*, 70, pp. 1055–96, 1982.
- [2] I. Daubechies & T. Paul, "Time-Frequency Localisation Operators: A Geometric Phase Space Approach II. The use of dilations and translations," *Inverse Problems*, vol. 4, pp. 661–80, 1988.
- [3] S. C. Olhede and A. T. Walden, "Generalized Morse Wavelets," *IEEE Trans. Signal Processing*, vol. 50, pp. 2661–70, 2002.
- [4] Lilly, J. M. & Park, J., "Multiwavelet spectral and polarization analyses of seismic records," *Geophys. J. Int.* **122**, 1001–21, 1995.
- [5] J.-P. Antoine, R. Murenzi & P. Vandergheynst, "Directional Wavelets Revisited: Cauchy Wavelets and Symmetry Detection in Patterns," *Applied and Computational Harmonic Analysis*, vol. 6, pp. 314–45, 1999.
- [6] L. A. Vese & S. J. Osher, "Modeling Textures with Total Variation Minimization and Oscillating Patterns in Image Processing," *J. Scien. Comp.*, vol. 19, pp. 553–72, 2003.
- [7] D. L. Donoho, "Tight frames of k plane ridges and the Problem of Representing Objects that are Smooth away from d dimensional singularities in R^n ," *Proc. of the Nat. Acad. of Science of the USA*, vol. 96, pp. 1828–33, 1999.
- [8] B. Boashah, "Estimating and Interpreting the Instantaneous Frequency of a Signal-Part; Part I: Fundamentals, II: Algorithms," *Proceedings of the IEEE*, **80(4)**, pp. 519–569, 1992.
- [9] M. Felsberg & G. Sommer, "The monogenic signal," *IEEE Trans Signal Proc*, vol. 49, pp. 3136–3144, 2001.
- [10] Bülow T. & Sommer G. (2001), "Hypercomplex signals – a novel extension of the analytic signal to the multidimensional case," *IEEE Trans Signal Proc*, **49**, pp. 2844–2852, 2001.
- [11] S. L. Hahn, "Multidimensional Complex Signals with Single-Orthant Spectra," *Proc. IEEE*, **80**, pp. 1287–1300, 1992.
- [12] C. A. Deavours, "The Quaternion Calculus," *The American Mathematical Monthly*, **80(9)**, pp. 995–1008, 1973.
- [13] M. Holschneider, *Wavelet: an analysis tool*, Oxford Science Publications, Oxford, UK. 1998.
- [14] C. Gonnet & B. Torresani, "Local frequency analysis with two-dimensional wavelet transform," *Signal Processing*, vol. 37, pp. 389–404, 1994.
- [15] W. L. Chan, H. Choi & R. Baraniuk, "Directional Hypercomplex Wavelets for Multidimensional Signal Analysis and Processing," *IEEE International Conference on Acoustics, Speech, and Signal Processing (ICASSP)*, Houston, TX, May, 2004.

- [16] F. C. A. Fernandes, R. L. C. van Spaendonck and C. S. Burrus, "Multidimensional, Mapping-Based Complex Wavelet Transforms," *IEEE Trans. Image Proc.*, vol. 14, pp. 110–24, 2005.
- [17] S. L. Hahn and K. M. Snopek, "Wigner Distributions and Ambiguity Functions of 2-D Quaternionic and Monogenic Signals," *IEEE Trans. Signal Proc.* vol. 53, pp. 3111–28, 2005.
- [18] D. Van De Ville, W. Philips, I. Lemahieu, "On the N-dimensional extension of the discrete prolate spheroidal window," *IEEE Signal Proc. Let.*, vol. 9, pp. 89–91, 2002.
- [19] F. J. Simons, R. D. van der Hilst RD, & M. T. Zuber, "Spatiospectral localization of isostatic coherence anisotropy in Australia and its relation to seismic anisotropy: Implications for lithospheric deformation," *J. Geophys. Res. – Sol. Ea.* vol. 108 (B5): art. no. 2250. 2003.
- [20] S. Dahlke & P. Maass, "The Affine Uncertainty Principle in One and Two Dimensions," *Computers Math. Applic.*, vol. 30, pp. 293–305, 1995.
- [21] M. Abramowitz & I. A. Stegun (ed), *Handbook of Mathematical Functions*, 9th printing Dover, New York: USA, 1972.
- [22] N. W. McLachlan, *Bessel functions for engineers*, Clarendon Press, Oxford, UK, 1955.
- [23] M. Felsberg & G. Sommer, "Structure Multivector for Local Analysis of Images." *Technical Report Bericht No 2001*, Christian Albrechts Universität, Kiel, 2001.
- [24] J. P. Havlicek, D. S. Harding and A. C. Bovik, "The Multicomponent AM-FM Image Representation," *IEEE Transactions on Image Processing*, vol. 5, pp. 1094–1100, 1996.
- [25] A. C. Bovik, N. Gopal, T. Emmoth & A. Restrepo, "Localized Measurement of Emergent Image Frequencies by Gabor Wavelets," *IEEE Trans. Signal Processing*, vol. 38, pp. 691–712, 1992.

APPENDIX

A: ORTHOGONALITY RELATIONS

We know that if we choose $c = (2l + 1)/m - 1$ [3, p. 2663] then

$$\begin{aligned}
 \int_{-\infty}^{\infty} \Psi_{n_1}^{(e)}(f) \Psi_{n_2}^{(e)}(f) df &= 2A_{n_1;l,m} A_{n_2;l,m} \int_0^{\infty} (2\pi |f|)^{2l} e^{-2(2\pi |f|)^m} L_{n_1}^c(2(2\pi |f|)^m) L_{n_2}^c(2(2\pi |f|)^m) df \\
 &= A_{n_1;l,m} A_{n_2;l,m} \int_0^{\infty} (s/2)^{(2l+1)/m-1} e^{-s} L_{n_1}^c(s) L_{n_2}^c(s) \frac{ds}{m} \\
 &= \delta_{n_1, n_2}.
 \end{aligned} \tag{64}$$

Consider the two-dimensional integral of two dimensional wavelets

$$\begin{aligned}
 \langle \psi_{n_1}^{(e)}, \psi_{n_2}^{(e)} \rangle &= \frac{1}{\pi} \int_{-\infty}^{\infty} \int_{-\infty}^{\infty} A_{n_1;l,m} (2\pi f)^l e^{-(2\pi f)^m} L_{n_1}^{c'}(2(2\pi f)^m) A_{n_2;l,m} (2\pi f)^l e^{-(2\pi f)^m} L_{n_2}^{c'}(2(2\pi f)^m) df_1 df_2 \\
 &= 2 \int_0^{\infty} A_{n_1;l,m} A_{n_2;l,m} (2\pi f)^{2l+1} e^{-2(2\pi f)^m} L_{n_1}^{c'}(2(2\pi f)^m) L_{n_2}^{c'}(2(2\pi f)^m) df \\
 &= A_{n_1;l,m} A_{n_2;l,m} \int_0^{\infty} (s/2)^{(2l+2)/m-1} e^{-s} L_{n_1}^{c'}(s) L_{n_2}^{c'}(s) \frac{ds}{m} \\
 &= \delta_{n_1, n_2}.
 \end{aligned} \tag{65}$$

Also note that

$$\begin{aligned} \langle \psi_{n_1}^{(l)}, \psi_{n_2}^{(l)} \rangle &= \frac{1}{\pi} \int_{-\infty}^{\infty} \int_{-\infty}^{\infty} A_{n_1;l,m} (2\pi f)^l e^{-(2\pi f)^m} L_{n_1}^{c'} (2(2\pi f)^m) \\ &\quad A_{n_2;l,m} (2\pi f)^l e^{-(2\pi f)^m} L_{n_2}^{c'} (2(2\pi f)^m) \frac{f_l^2}{f_1^2 + f_2^2} df_1 df_2, \quad l = 1, 2. \end{aligned}$$

This implies that $\langle \psi_{n_1}^{(1)}, \psi_{n_2}^{(1)} \rangle + \langle \psi_{n_1}^{(2)}, \psi_{n_2}^{(2)} \rangle = \langle \psi_{n_1}^{(e)}, \psi_{n_2}^{(e)} \rangle = \delta_{n_1, n_2}$, and as $\Psi_n^{(e)}(\mathbf{f})$ is radially symmetric we may deduce that

$$\langle \psi_{n_1}^{(1)}, \psi_{n_2}^{(1)} \rangle = \langle \psi_{n_1}^{(2)}, \psi_{n_2}^{(2)} \rangle, \quad (66)$$

and thus

$$\langle \psi_{n_1}^{(1)}, \psi_{n_2}^{(1)} \rangle = \frac{1}{2} \delta_{n_1, n_2}. \quad (67)$$

Finally, note that

$$\begin{aligned} \langle \psi_{n_1}^{(e)}, \psi_{n_2}^{(1)} \rangle &= \frac{1}{\pi} \int_{-\infty}^{\infty} \int_{-\infty}^{\infty} A_{n_1;l,m} (2\pi f)^l e^{-(2\pi f)^m} L_{n_1}^{c'} (2(2\pi f)^m) \\ &\quad A_{n_2;l,m} (2\pi f)^l e^{-(2\pi f)^m} L_{n_2}^{c'} (2(2\pi f)^m) (-i) \frac{f_1}{f_1^2 + f_2^2} df_1 df_2 \\ &= 0, \end{aligned} \quad (68)$$

due to the integral of an odd function over a symmetric region being zero. Similarly

$$\langle \psi_{n_1}^{(e)}, \psi_{n_2}^{(2)} \rangle = 0, \quad \langle \psi_{n_1}^{(1)}, \psi_{n_2}^{(2)} \rangle = 0. \quad (69)$$

B: CALCULATION OF STATISTICAL PROPERTIES

Define the discrete Fourier transform of the noise ϵ_{x_1, x_2} ,

$$\mathcal{E}(f_1, f_2) = \sum_{x_1=0}^{N_1-1} \sum_{x_2=0}^{N_2-1} \epsilon_{x_1, x_2} e^{-2j\pi(f_1 x_1 + f_2 x_2)}. \quad (70)$$

As the wavelet transform at any angle θ can be formed from linear combinations of the wavelet transform at $\theta = 0$, in the way outlined in section VI, we need only calculate the properties at $\theta = 0$. We have:

$$\begin{aligned} &E \left(w_{n_1}^{(e)}(\boldsymbol{\xi}; \epsilon) w_{n_2}^{(e)*}(\boldsymbol{\xi}; \epsilon) \right) \\ &= \frac{a^2 \sigma_\epsilon^2}{N_1^2 N_2^2 \Delta_1^2 \Delta_2^2} \sum_{l_1=-N_1'}^{N_1'-1} \sum_{l_2=-N_2'}^{N_2'-1} \sum_{l_3=-N_1'}^{N_1'-1} \sum_{l_4=-N_2'}^{N_2'-1} \delta_{l_1, l_3} \delta_{l_2, l_4} e^{2j\pi(b_1(l_1-l_3)+b_2(l_2-l_4))} \\ &\quad \Psi_{n_1} \left(a \sqrt{\frac{l_1^2}{N_1^2 \Delta_1^2} + \frac{l_2^2}{N_2^2 \Delta_2^2}} \right) \Psi_{n_2} \left(a \sqrt{\frac{l_3^2}{N_1^2 \Delta_1^2} + \frac{l_4^2}{N_2^2 \Delta_2^2}} \right) \\ &\approx a^2 \sigma_1^2 \sigma_2^2 \int_{-\frac{1}{2\Delta_1}}^{\frac{1}{2\Delta_1}} \int_{-\frac{1}{2\Delta_2}}^{\frac{1}{2\Delta_2}} \Psi_{n_1} \left(a \sqrt{f_1^2 + f_2^2} \right) \Psi_{n_2} \left(a \sqrt{f_1^2 + f_2^2} \right) df_1 df_2 \end{aligned} \quad (71)$$

$$= \sigma_\epsilon^2 \delta_{n_1, n_2}, \quad (72)$$

where the last line follows from Eq. (65). Similarly

$$\text{Cov} \left(w_{n_1}^{(1)}(\boldsymbol{\xi}; \epsilon), w_{n_2}^{(1)}(\boldsymbol{\xi}; \epsilon) \right) \quad (73)$$

$$\approx a^2 \sigma_\epsilon^2 \int_{-\frac{1}{2\Delta_1}}^{\frac{1}{2\Delta_1}} \int_{-\frac{1}{2\Delta_2}}^{\frac{1}{2\Delta_2}} \Psi_{n_1} \left(a\sqrt{f_1^2 + f_2^2} \right) \Psi_{n_2} \left(a\sqrt{f_1^2 + f_2^2} \right) \frac{f_1^2}{f_1^2 + f_2^2} df_1 df_2 \quad (74)$$

$$= \frac{1}{2} \sigma_\epsilon^2 \delta_{n_1, n_2}. \quad (75)$$

following from Eq. (67), and likewise

$$\text{Cov} \left(w_{n_1}^{(2)}(\boldsymbol{\xi}; \epsilon), w_{n_2}^{(2)}(\boldsymbol{\xi}; \epsilon) \right) = \frac{1}{2} \sigma_\epsilon^2 \delta_{n_1, n_2}. \quad (76)$$

Furthermore,

$$\text{Cov} \left(w_{n_1}^{(e)}(\boldsymbol{\xi}; \epsilon), w_{n_2}^{(1)}(\boldsymbol{\xi}; \epsilon) \right) \quad (77)$$

$$\begin{aligned} &= E \left(w_{n_1}^{(e)}(a, 0, b_1 \Delta_1, b_2 \Delta_2; \epsilon) w_{n_2}^{(1)*}(a, 0, b_1 \Delta_1, b_2 \Delta_2; \epsilon) \right) \\ &\approx a^2 \sigma_\epsilon^2 \int_{-\frac{1}{2\Delta_1}}^{\frac{1}{2\Delta_1}} \int_{-\frac{1}{2\Delta_2}}^{\frac{1}{2\Delta_2}} \Psi_{n_1} \left(a\sqrt{f_1^2 + f_2^2} \right) \Psi_{n_2} \left(a\sqrt{f_1^2 + f_2^2} \right) \frac{f_1}{\sqrt{f_1^2 + f_2^2}} df_1 df_2 \\ &= 0, \end{aligned} \quad (78)$$

following from Eq. (68), likewise $\text{Cov} \left(w_{n_1}^{(e)}(\boldsymbol{\xi}; \epsilon), w_{n_2}^{(1)}(\boldsymbol{\xi}; \epsilon) \right) = 0$ according to (69), and finally

$$\text{Cov} \left(w_{n_1}^{(1)}(\boldsymbol{\xi}; \epsilon), w_{n_2}^{(2)}(\boldsymbol{\xi}; \epsilon) \right) \quad (79)$$

$$\begin{aligned} &= E \left(w_{n_1}^{(1)}(a, 0, b_1 \Delta_1, b_2 \Delta_2; \epsilon) w_{n_2}^{(2)*}(a, 0, b_1 \Delta_1, b_2 \Delta_2; \epsilon) \right) \\ &\approx a^2 \sigma_\epsilon^2 \int_{-\frac{1}{2\Delta_1}}^{\frac{1}{2\Delta_1}} \int_{-\frac{1}{2\Delta_2}}^{\frac{1}{2\Delta_2}} \Psi_{n_1} \left(a\sqrt{f_1^2 + f_2^2} \right) \Psi_{n_2} \left(a\sqrt{f_1^2 + f_2^2} \right) \frac{f_1 f_2}{f_1^2 + f_2^2} df_1 df_2 \\ &= 0, \end{aligned} \quad (80)$$

following from Eq. (69). This completes the covariance calculations for the distribution.